American Society of
Mechanical Engineers

ASME Accepted Manuscript Repository

Development of a Novel Ground Test Facility for Aircraft Environmental Control System

Shafayat H. Chowdhury, Fakhre Ali, Ian K. Jennions

IVHM Centre, Cranfield University, Bedfordshire, MK43 0AL, United Kingdom

shafayat.chowdhury@cranfield.ac.uk

f.ali@cranfield.ac.uk

i.jennions@cranfield.ac.uk

Abstract

In this paper the development and experimental investigation of a Boeing 737 aircraft Environmental Control System (ECS) passenger air conditioner (PACK) has been reported. The PACK is the heart of the ECS that conditions bleed air prior to supplying it to the cabin and avionics bay. Its capability to mask fault occurrences has resulted in increased unscheduled maintenance of the system. As such it has been a key research topic to understand PACK performance characteristics in order to support an accurate diagnostic solution. This paper is a continuation of the authors' work on the development of a systematically derived PACK simulation model and reports the overall development and qualification of a novel in-situ ground test facility (GTF) for the experimental investigation of a B737-400 aircraft PACK under various operating modes, including the effect of trim air system. The developed GTF enables the acquisition of the temperature, pressure and mass flow data throughout the PACK. The overall process of instrumentation selection, installation, sensor uncertainty, and testing in terms of data repeatability and consistency has been reported. The acquired data is then employed to conduct a verification and validation of the SESAC simulation framework. The reported research work therefore enables the advancement in the level of scientific understanding corresponding to the ECS PACK operation under real operating conditions, and therefore supports the development of a robust simulation framework for ECS fault diagnostics at system level.

Nomenclature

Acronyms

ACM	Air Cycle Machine
APU	Auxiliary Power Unit
B737	Boeing 737
BFSL	Best Fit Straight Line
CHX	Condensing Heat Exchanger
CMP	Compressor
ECS	Environmental Control System
FSS	Full-Scale Span
GTF	Ground Test Facility
HPWS	High Pressure Water Separator
LC	Load Condition
PACK/PCK	Passenger Air Conditioner
pTCV	Post TCV
PV	PACK Valve
PHX	Primary Heat Exchanger
RAM	RAM- ambient air
RC	Reference Case
RH	Relative Humidity
RHX	Reheating Heat Exchanger
SESAC	Simscape ECS Simulation under All Conditions

SHX	Secondary Heat Exchanger
TCV	Temperature Control Valve
TRB	Turbine
WS	Water Separator

Symbols

A	Area
D_H	Hydraulic diameter
f	Friction factor
k	Loss coefficient
L	Length
$\dot{m}$	Mass Flow
P	Pressure
T	Temperature
v	Velocity

Subscript

amb	Ambient
Cab	Cabin
c	Cold
d	Dynamic
h	Hot
i	Inlet

o	Outlet
pri	Primary
s	Static
sec	Secondary
t	Total

Greek Symbols

δ	Uncertainty Error
ϵ	Effectiveness
μ	Mean Value
ρ	Density
σ	Standard Deviation
τ	Shear stress

1 Introduction

The Environmental Control System (ECS) provides pressurised air to the anti-ice system and regulates cabin temperature (T), pressure (P) and humidity (RH). To serve its purpose, it utilises: (i) Bleed Air System, (ii) Passenger Air Conditioner (PACK) and (iii) Air Distribution System. The PACK is the core module of the ECS and consists of various components which are prone to degradation [1].

To maximise aircraft operational availability by providing fleet care, the original equipment manufacturers are actively working on improving diagnostic tools to help minimise maintenance costs. The Boeing company has reported the Environmental Control System (ECS) of legacy aircraft such as the Boeing 737 to be one of the major drivers for maintenance which demands cost-effective and accurate diagnostic solutions [1]. The diagnostics of such ECS systems becomes challenging due to the lack of data that can be used to study fault occurrences and their propagation. In addition to that, the capability of the flow control valves to mask fault occurrences makes the diagnostic process even more challenging. It therefore necessary to understand PACK performance under different operating conditions, including the fault occurrences and, consequently, its impact on the overall PACK performance characteristics. This knowledge will allow identification of component health state indicating parameters that can support the development of effective diagnostic tools.

This has led to the growing interest in the industry and academia to initiative research to enable the engineering and scientific understanding of the PACK system [2]–[7]. The literature suggests that component level performance assessment has been mostly targeted towards heat exchangers, as they were deemed to be a key component to match cabin temperature demand. It is of paramount importance to also study the interdependencies of the components within the system to understand the behavioural characteristics of fault occurrence and its propagation. This leads to identification of appropriate sensor installation locations to perform accurate diagnostics.

Based on recent literature review conducted by the authors on the ECS simulation and diagnostics [8], there is an evident gap in the open literature with regards to in-depth

system-level performance analysis of the ECS as well as its in-situ experimental testing. In the last four decades a handful of ECS simulation models have emerged in the literature, including: (i) EASY5 [9], [10], (ii) FLECS [11], [12], (iii) Flowmaster [13], [14], (iv) Dymola [10], [15] and (v) SESAC [16], [17]. Among these models SESAC was purposefully developed by Cranfield University's IVHM Centre to support condition-based monitoring and diagnostics of civil aircraft ECS with the capability to introduce degradation in the simulation. It is interesting to note that these models have not been comprehensively verified using test data across each component, because there is very limited data coming from these legacy systems due to a lack of sensors. With the exception of SESAC, the simulation models have been primarily used for design and analysis purposes. Also, in order to be used for diagnostic purposes the models require experimental verification and validation at a system level. It is noted that the verification and validation of the models have not been done comprehensively.

To attain reliability on the model's capability to accurately estimate PACK performance under healthy and degraded scenarios, a systematic verification and validation is necessary. As reported by Childs et al, an experimental rig was developed using a Hawk ECS to perform ECS model verification [18]. Similarly, an experimental investigation was conducted on a Boeing 737-200 aircraft to collect temperature, pressure and valve position to support verification of an ECS thermodynamic model [19]. These two ECS cases are similar in terms of their architecture, and both have a low-pressure water separator system.

However, as reported in October 2020, there are only 60 Boeing 737-200 aircraft in service. This is significantly fewer than the 6393 next generations (NG) variant, the -600, -700, -800, and -900 [20]. Based on the sheer number of NGs still in service, and that the latest variant Boeing 737 MAX uses a pneumatic ECS with a high-pressure water separator (HPWS), there is a need for a 737 ECS Ground Test Facility (GTF) to be used for studying system performance in terms of temperature (T), pressure (P), mass flow ($\dot{m}$) and relative humidity (RH). Such a facility would also play a significant role in supporting future research on sensor optimisation and fault simulation analysis.

6

1.1 Scope of Present Work

In the light of the literature review reported by the authors in [8], there exist a gap in terms of the availability of experimental ECS data in order to support the accurate simulation of the ECS under-wide range of operating conditions. This paper reports the step by step development and qualification of a GTF for the in-situ experimental investigation of a B737-400 aircraft ECS under various operating modes, including the effect of trim air system. The developed GTF enables the acquisition of the temperature, pressure and mass flow data throughout the ECS PACK. The overall process of instrumentation selection, installation and testing in terms of data repeatability and consistency has been reported. The acquired data is then employed to conduct a verification and validation of the SESAC simulation framework. The reported research work therefore enables the advancement in the level of scientific understanding corresponding to the ECS PACK operation under real operating conditions, and therefore supports the development of a robust simulation framework.

2 Background - Overview of PACK Operation and SESAC

The ECS uses multiple subsystems (i.e. bleed air system, PACK and air distribution system) including a control system regulating flow across the system to meet temperature and pressure requirements in cockpit, cabin and avionics bay. The bleed system provides the pressurised air to the PACK for conditioning. Part of the bleed mass flow before entering the PACK is taken out to drive the ram turbo-fan to drive cold ambient air over the heat exchangers in the PACK to enable pre-cooling of the bleed air. After conditioning of the bleed air in the PACK, the air is mixed with trim and recirculating air from the cabin in the mixing manifold before it is distributed in different zones of the aircraft.

The PACK is the primary system for conditioning the flow within the ECS, which makes it the focus of this study. Figure 1 shows a schematic of a single PACK in the B737-400. It consists of valves, heat exchangers, an air-cycle machine (ACM) and HPWS. Following the sequence shown in Figure 1, the PACK receives bleed air at high temperature and pressure, primary cooling takes place in the PHX, and secondary cooling takes place in the SHX, after the flow is compressed. Cold ram air, which originates from outside the

aircraft, flows through the ram air duct and, after being used as a heat sink for PHX and SHX, is deposited back into the aircraft's airstream. After the SHX the temperature of the bleed air has been substantially reduced and the high pressure flow is expanded through a turbine, after passing through the HPWS to control humidity. At the outlet of the turbine the air temperature can potentially drop below freezing and, if this occurs, it is addressed by mixing in part of the bypass hot bleed flow through the TCV. The mixing of this air is controlled in order to match the PACK outlet temperature against the cabin demand.
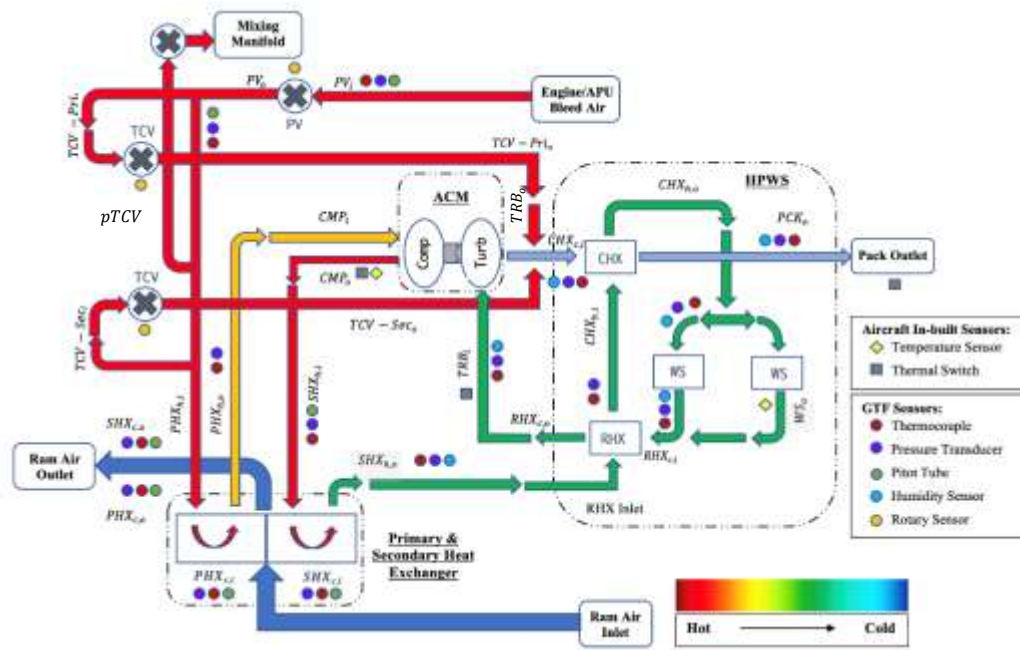

Figure 1 B737-400 PACK schematic with sensor installation locations

2.1 PACK Temperature Control

The cabin temperature demand can be regulated through the input dials mounted on the P5 overhead panel within the cockpit [21]. On the B737-400 aircraft, the cabin temperature demand can be regulated within the range of 18°C to 30°C. The PACK zone controller unit receives input from the P5 overhead panel, sensors listed in Table 1, and temperature sensors located inside the cabin, to meet target temperature in the cabin.

The PACK temperature control primarily acts in two ways: (i) by controlling the cold ram air supply by regulating the ram air inlet modulating flap, and (ii) by controlling the PACK outlet temperature through the hot bypass stream by regulating the TCV, see

Figure 1. It is necessary to regulate the PHX, SHX and turbine outlet temperature to meet the lowest cabin demand (out of the three zones) using the temperature sensors listed in Table 1. These two inbuilt temperature sensors, at the CMP_o and WS_o, support the control system with necessary feedback to control the temperature throughout the PACK, and its compliance against the demanded cabin temperature.

Table 1 Inbuilt Temperature sensors for PACK temperature control

Temperature Sensor	Location	Threshold
RAM air temperature sensor	Compressor outlet duct (CMP_o)	Regulates RAM mass flow to maintain the Compressor outlet temperature to as near 110 ºC as possible
PACK temperature sensor	Water extractor outlet duct (WS_o)	Regulates TCV opening to maintain the lowest temperature demand from the zone

2.2 Trim System

In addition to PACK temperature control, the P5 panel also provides control over the trim system main valve, which can be switched on and off. As illustrated in Figure 2, the function of the trim system is to ensure the supply of hot air to the cabin air distribution ducts, this allows the adjustment in the temperature supplied to each cabin compartment. For example, both forward and aft passenger cabins can be set to meet $24°C$ temperature demand, however, depending on the heat load of each compartment, the required temperature supply can vary in order to meet the demanded temperature. As shown in Figure 2, following the stated station numbering, at station 1, the bleed flow is supplied by the APU, at the PACK valve (station 2) the flow is supplied to the passenger air conditioning PACK. As illustrated, immediately downstream of the station 2, part of the flow is by passed through the TCV into the passenger air conditioning PACK (labelled as station 2.1), and at the upstream of the PACK inlet (station 2.2) part of the PACK inlet

flow is extracted and is fed in to the trim air system. Switching on the trim system would therefore allow the PACK-zone controller to regulate (open or close) the trim valve based on the cabin temperature sensor feedback. The amount of mass flow going through the air conditioning PACK is therefore strongly dependant on the status of the trim valve, which can consequently affect the performance characteristics of the components mounted within the air conditioning PACK i.e. PHX, SHX, ACM, HPWS.
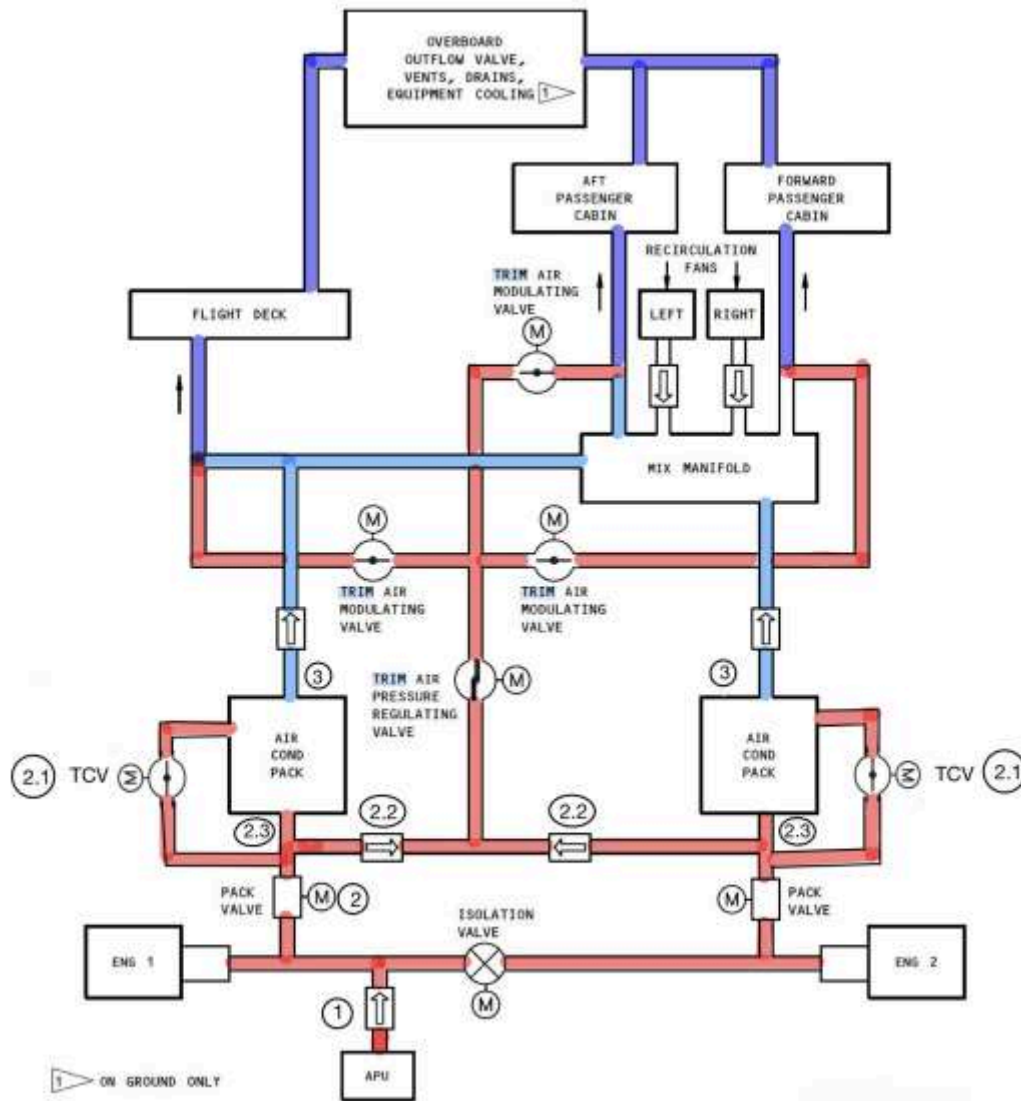

Figure 2 737- 400 ECS Schematic (red, blue and purple annotation represent bleed air, conditioned air and air inlet to the flight deck and cabin respectively), adopted and reproduced from Boeing 737-400 AMM [22]

2.3 ECS Simulation Framework – SESAC

SESAC is a MATLAB based ECS component library developed by Jennions et al [16], enabling by a drag-and-drop interface. The authors have reported detailed analysis of PACK performance at cruise using data provided by Boeing. Figure 3 shows the SESAC PACK simulation model of a B737-800 developed at IVHM centre [16]. The model configuration of the B737-800 in terms of the architecture and flow sequence mirrors the B737-400 schematic presented in Figure 1.

The PACK receives input bleed air at high temperature and pressure from the engine (via the bleed air system), the quantity of which is controlled by the PACK valve (PV). The overall model is comprised of many different modules, and virtual sensors for the control logic. Immediately downstream of the PV, the flow is split into two streams. Part of the air flow passes through the cold stream of the PACK, part of it is bypassed through the TCV and mixed at the TRB_o In the cold stream, the flow proceeds through the heat exchangers, which use the ram air as a heat sink to drop the temperature. The compressor, positioned between the heat exchangers, increases the air pressure in order to maximise the expansion through the turbine. The HPWS is composed of a reheater, condenser and water extractor, allowing the extraction of water content prior to the expansion of the air in the turbine.
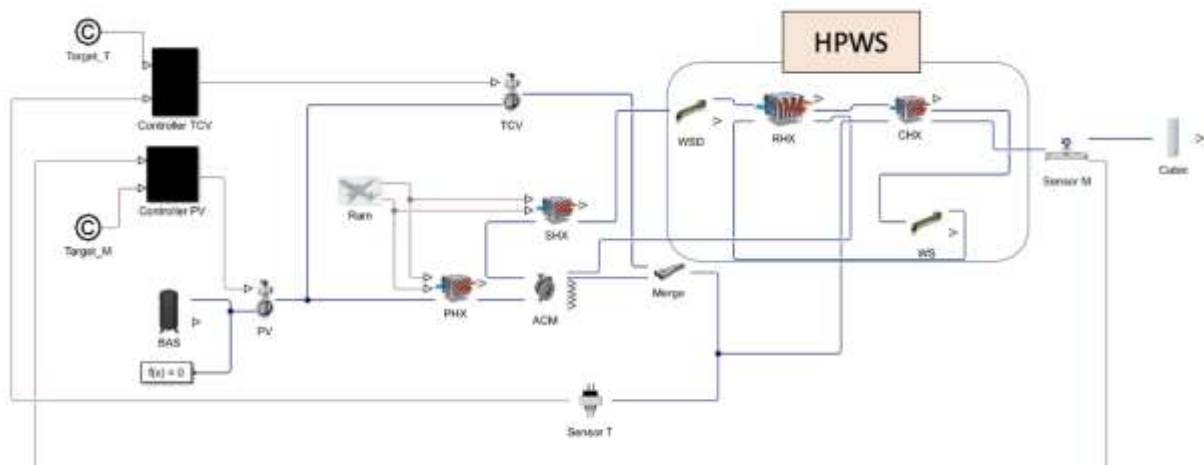

Figure 3 SESAC Simulation Model for B737-800 [16]

There are two control loops in the system, one for temperature and one for flow (Figure 3). A (virtual) temperature sensor placed at the outlet of the merge provides a feedback signal to the controller of the TCV, which regulates the TCV valve angle to deliver the required hot mass flow. Downstream of this is a (virtual) mass flow sensor, placed immediately downstream of the merge component providing a feedback signal to the PV mass flow controller, which regulates the overall mass flow.

3 Development of the B737-400 Ground Test Facility

Cranfield University owns a Boeing 737, which is used for education and research. The research emphasis is to turn the plane into a GTF for a number of aircraft systems. In the current work the emphasis is on the ECS, and the left-hand side PACK was selected for experimental work. In this section the selection of sensors is summarised for completeness (previously reported by the authors [23]), along with the operational envelope of the experiments and the classification of data collection.

3.1 Sensor Selection and Installation

The PACK functionality is to condition the bleed air supplied by the Engines/APU which is generally at a very high temperature and pressure. Therefore, one of the key requirements for the sensor selection is to comply with the operating temperature and pressure at various locations. Table 2 provides the list and the specifications of the selected sensors for measuring T, P, RH and valve angles. The maximum operating temperature of the pressure transducers (125°C) falls well below the expected temperature (approximately $180°C$) at the PV_i, PV_o and $PHX_{h,i}$ stations [16]. Therefore, to protect the transducers from overheating at these stations, temperature isolation coils [24] were used. These coils are tube (0.635cm of diameter) made of stainless steel and specification suggests that a tube length of 7.62cm can drop the source temperature from 200°C to approximately 93°C through heat transfer into ambient air of temperature 38°C [25].

Table 2 List of sensors and their specifications defined by manufacturer

Manufacturing P/N	Type	Range	Temperature Range	Accuracy	Offset error	Total Error Band	Reference
Honeywell PX2EN1XX100 PSAAX	Relative pressure	101.352 to 689 kPa	-40 to +125°C	±0.25% BFSL of FSS	±1% of FSS	±2% of FSS	[26]
Honeywell PX2EF1XX050 PAAAX	Absolute pressure	0 to 344 kPa	-40 to +125°C	±0.25% BFSL of FSS	±1% of FSS	±2% of FSS	[26]
Omega, K-type Thermocouple K-L-1-6-40-G1/8-T-2	Temperature	0 to 400°C		±1.5°C	-	-	[27]
TE Connectivity HTM2500LF	Relative Humidity	0 to 100% RH	-40 to +85°C	±5%	-	-	[28]
Active Sensor MHR5210 CV-090	Rotational angle	0 to 90°	0 to +150°C	±0.11%	-	-	Calibration test report provided by manufacturer

Monarch Engineering Services LTD conducted the disassembly of the left-side PACK, from which the PV, TCV, HXs, ACM and HPWS came out as a single unit. Appropriate safety measures were taken, such as pulling out circuit brakers, and covering and labelling ducts. The sensor bosses were manufactured in a laboratory and welded on the target site. Sensors were mostly installed on the ducts, and locations were selected based on the space available. The existing sensor boss available on the HPWS was utilised for humidity sensor installation by designing appropriate T-junctions and using compression fittings. The compression fittings were tested in the lab for suitability [23]. Sensor installation plates were manufactured and welded on the HX inlet (RAM side) and RAM air outlet duct. The rotary sensors were installed on the PV, Primary TCV and

Standby TCV. Removable rigs were designed and manufactured to connect the sensors with the pivotal point of the butterfly valves. After reassembling the PACK with all the sensors installed, the data acquisition unit (DAQ) was installed with all the sensors connected, as shown in Figure 4. An ethernet cable and a power supply cable were taken out from the bay, completing the hardware assembly of the B737 GTF.

The ECS was tested in a systematic approach for functionality. The APU was powered and allowed to reach steady-state (5 minutes time allowance). Electrical components were turned on to put a 100amp load on the APU. The ECS left-side PACK was then powered on for 5 minutes, after which ducts, and the replaced seals, were manually tested for leakages [23].

Figure 4 Ground test facility of the Boeing 737-400, Left-side PACK data collection

3.2 Definition of the Operational Envelope for Experimentation

The GTF is developed to conduct experimental testing of the PACK, with the aircraft on the ground, under various operating conditions and functional scenarios. The scope of this paper covers the experimental testing of the PACK under a wide range of operating conditions, i.e. hot and cold demand, trim on and off. Cold demand represents passenger cabin temperature at 18 ºC and under hot demand at 24 ºC. The overall experimental tests were conducted over a number of different days with varying ambient conditions. The start-up sequence starts with powering up the APU. Once steady exhaust gas temperature is obtained from the APU, the bleed valve is energised from the P5 overhead

panel in the cockpit. Subsequently, the left-side PACK is turned on and operated for 5 minutes, similar to the functionality test, then data collection begins in order to capture the steady-state operating data. Table 3 shows the operating conditions of the seven sets of data, labelled as reference cases (RCs), taken during the experimental program. These RCs account for data collected under different ambient and PACK operating scenarios and will be used in Sections 5 and 6 to support GTF qualification and V&V of SESAC respectively.

Table 3 Experimental test reference case classification

Reference Cases	Trim Status	Cabin Demand	Cabin Demand (°C)	T_{amb}(°C)
RC1	On	Hot	24	11.5
RC2	On	Hot	24	9.0
RC3	On	Hot	24	5.5
RC4	On	Cold	18	6.5
RC5	Off	Cold	18	6.5
RC6	On	Hot	24	5.5
RC7	Off	Hot	24	5.5

4 Uncertainty Analysis

In experimentation, every measurement is subjected to error as nothing is 100% perfect. Mathematically this phenomenon can be represented as:

$$\text{Measured Value} = \text{True Value} \pm \text{Total Error} \tag{1}$$

The total error can manifest itself in one of two ways: (i) Accuracy and (ii) Precision [29, p. 36]. Accuracy error shows how far away the measured value is from the true value, and precision error represents the total spread of data in a given population. The following section presents the calibration tests conducted to quantify the errors associated with the sensors.

4.1 Accuracy

The accuracy error based on the worst-case scenario of the pressure transducers and thermocouple are given by the manufacturer as shown in Table 2. To deduce the typical accuracy error associated with the sensor, laboratory tests were conducted on both the pressure transducers and thermocouples. The accuracy error is calculated as the difference between a known reading and measured data.

4.1.1 Pressure Transducers

The pressure acting on any surface is defined as the force acting per unit area of the surface. Based on this principle, pressure transducers are manufactured with a constant area diaphragm that undergoes deflection due to the force acting upon it. This deflection is measured and converted into an electrical output measured, in this experiment it's in volts [30]. Processing this electrical output provides an indication of the applied pressure. Inevitably the sensor readings are subject to offset, pressure non-linearity, hysteresis, non-repeatability, thermal effect on offset and thermal hysteresis errors [26].

The offset error refers to the start of the measuring range and can be higher or lower than actual [31]. The contributing factors in causing this error are pressure change frequency and amplitude, temperature fluctuations, material responses and environmental changes [32]. Before starting the APU and ECS all transducers should measure atmospheric pressure, any deviation from this being the offset. This offset, for all the pressure transducer locations, over a five day period, is shown in Table 4. It can be seen that the offset on each day varies across the transducers, and across the days, the maximum offset observed being 5.77 kPa. As per the specification provided by the manufacturer (Table 2), the maximum offset quoted for the relative pressure, at 25°C, was 6.89 kPa. The measured offset, as shown in Table 4, is recorded and used on each experimental data collection following the procedure suggested by the manufacturer [33].

Table 4 Offset error variation across each pressure transducer (kPa)

	PV_i	pTCV	$PHX_{h,o}$	CMP_o	$RHX_{h,o}$	$CHX_{h,o}$	WS_o	$RHX_{c,o}$	$Merge_o$	PCK_o
Day 1	2.35	1.64	3.63	4.4	5.42	3.69	4.14	1.29	3.91	2.31
Day 2	1.45	0.71	2064	3.59	4.51	2.83	3.31	0.26	3.06	1.39
Day 3	0.52	-0.84	1.19	1.25	1.67	1.59	1.05	1.49	0.19	0.49
Day 4	1.33	-0.69	-0.49	1.36	0.47	2.29	1.40	-0.13	1.38	1.31
Day 5	1.89	1.75	3.23	5.58	5.77	3.6	3.72	1.06	2.32	2.29

Referring to Table 2, the manufacturer has given the accuracy of the absolute and relative pressure transducers to be about 0.86kPa (0.25% of 345kPa) and 1.72kPa (0.25% of 689kPa) respectively, which includes pressure hysteresis, non-linearity, and non-repeatability errors. The pressure hysteresis, non-linearity and repeatability corresponds to the maximum deviation of the sensor reading from the actual value, total error in Eq.1.

To investigate accuracy further, a reference pressure kit [31] was used to apply a known pressure to the pressure transducer at room temperature of 20°C. The sensor data was recorded using the same data acquisition unit as on the aircraft. Figure 5 shows the load condition (LC) on the x-axis, applied pressure and measured pressure on the primary y-axis, and the difference between applied and measured pressure on the secondary y-axis. A maximum difference of approximately 0.58kPa and 0.6kPa pressure was observed in this test for both the absolute (50 psi) and relative (100 psi) pressure transducer respectively.
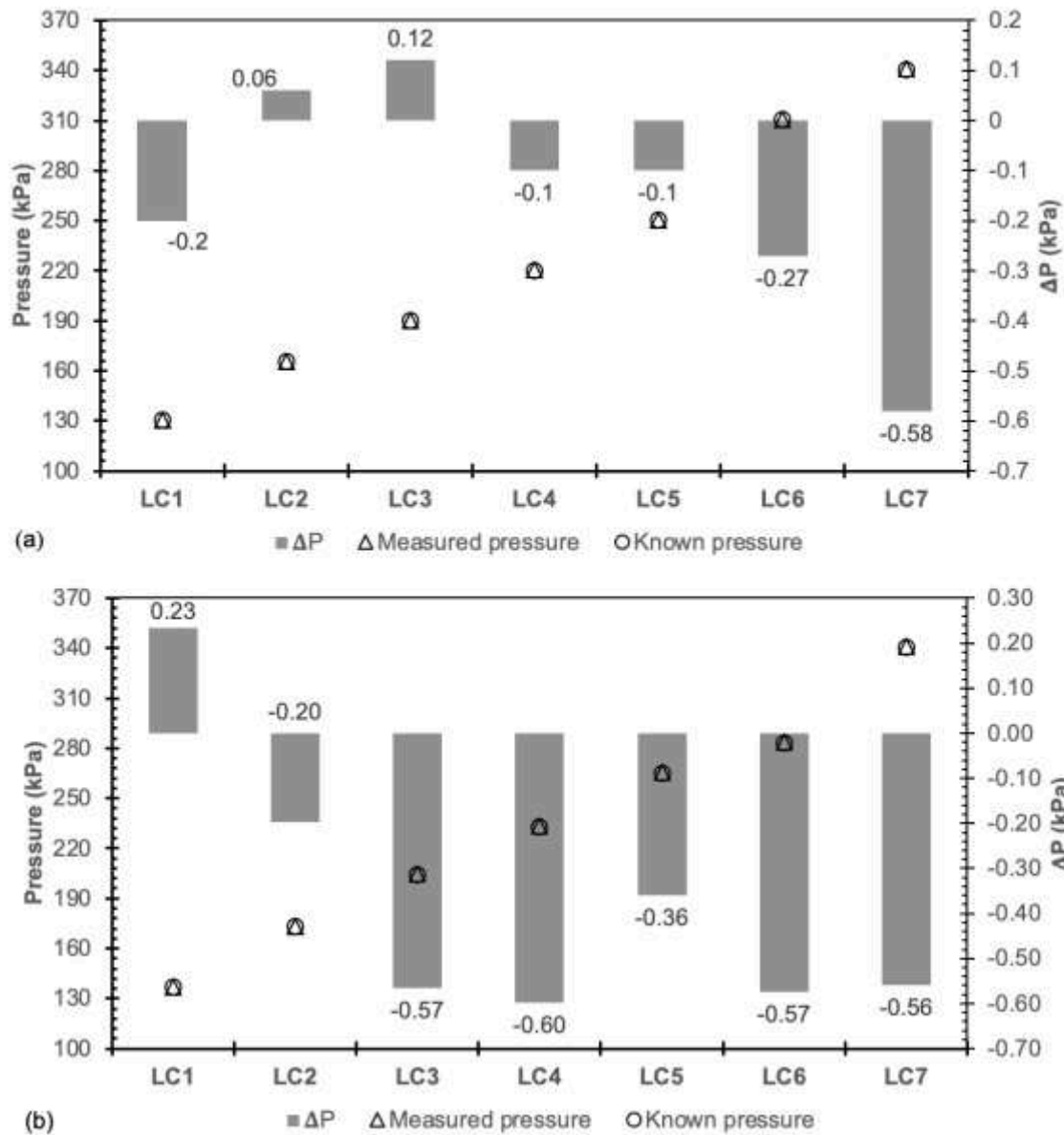
Figure 5 (a) Absolute pressure transducer and (b) relative pressure transducer error in pressure reading recorded under ambient temperature of 20°C.

In addition to conducting tests under room temperature, oven tests were conducted on the relative pressure transducer as they are installed at the high temperature stations across the PACK. As highlighted in section 3.1, due to the use of temperature isolation coil the temperature of the source is dropped to approximately 100°C, therefore, the transducer was tested under 53°C (midpoint) and 100°C (maximum expected

temperature at the transducer). Table 5 shows the tests result highlighting the applied load (true pressure), pressure readings (measured pressure) and the maximum ΔP between the true and measured value. The maximum ΔP, which can be attributed to the pressure non-linearity, hysteresis, and non-repeatability, is observed to be around -0.6kPa.

Table 5 Thermal control chamber pressure (kPa) test result with increased load at 53°C and 100°C operating temperatures

	53°C			100°C		
	True Pressure	Measured Pressure	ΔP	True Pressure	Measured Pressure	ΔP
Test 1	212.10	212.70	-0.6	212.10	211.97	0.13
Test 2	234.10	234.36	-0.26	234.10	234.56	-0.46
Test 3	289.10	288.90	0.20	289.10	288.84	0.26
Test 4	304.10	303.51	0.59	304.10	303.55	0.55

From the test results it has been deduced that the pressure transducers are far more accurate in comparison to the maximum accuracy specified by the manufacturer. The uncertainty (maximum error observed) for the absolute and relative pressure transducer is deduced to be ±0.58kPa and ±0.6kPa. The absolute pressure transducers are installed at the $CHX_{h,o}$, $RHX_{c,o}$, $Merge_o$, PCK_o and ram inlet-outlet and relative pressure transducers are installed across the rest of the stations across the PACK. As the uncertainty for both the transducers are seen to be almost identical, therefore ±0.6kPa of accuracy error will be used in rest of the paper.

4.1.2 Thermocouples

With the K-type thermocouple used here the technical specification suggests the accuracy to be within ±1.5°C [27]. In order to verify the accuracy of the thermocouple, an ice and boiling water test was conducted. Data was collected for 1 minute at 10Hz while the thermocouple was dipped in ice and then boiling water. It was noticed that the total

accuracy error in measuring the temperature of ice and boiling water was 0.14% and 0.04% respectively. The maximum difference between expected and thermocouple measurement is found to be -0.38K. This indicates that the thermocouples used in the experimentation are significantly more accurate than the pressure transducers.

4.2 Precision

The precision error of the sensor readings highlights the spread of a data sample. This error can occur due to unknown and unpredictable changes in the experiment or the environment, and it is unbiased and cannot be eliminated. Calculating the mean (μ) of the data collected at a steady state is used in experimentation to account for such unbiased error. Peters, C [34], mentioned in a book chapter that this error typically falls within one standard deviation (σ) with a 68% confidence interval. This is true if the data set is normally distributed at which case mean, median and mode are equal [35, p. 101].

To verify if the data sample is distributed normally, a histogram plot for different sample sizes was plotted, and is shown in Figure 6. Measured values are shown in blue, over three data collection times (30s, 1min, 2mins), and the best fit normal distribution from SPSS is shown as the bell curve. Overall there is only a very small change in pressure statistics across the three measuring times with the thermocouple readings showing more of a change (but again very small).
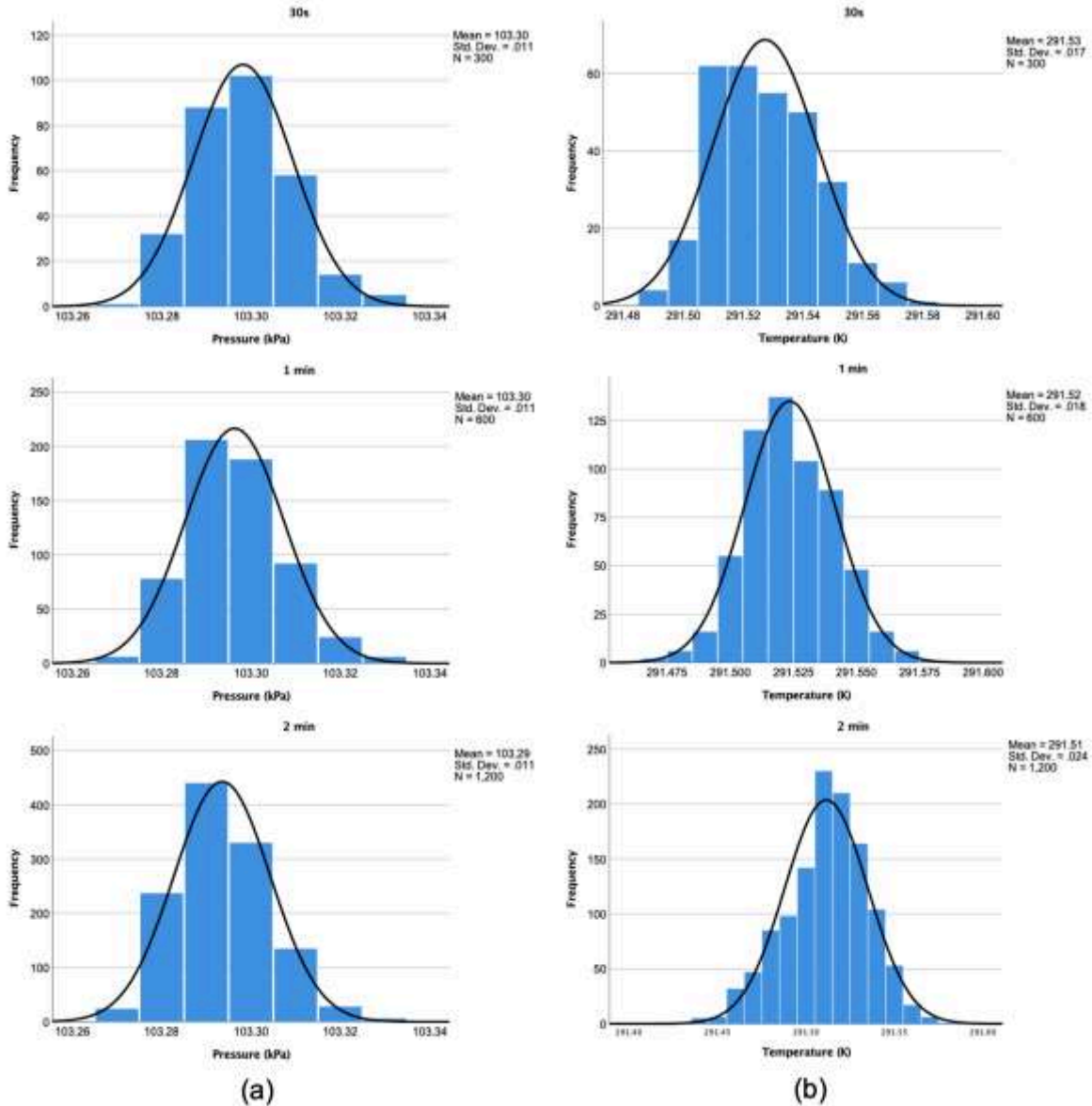
Figure 6 Histogram plots: (a) Pressure transducer and (b) Thermocouple

To verify normality of the data, the calculated mean, median and skewness value of the data samples are used, see Table 6. The skewness value is used to quantify the asymmetric nature of the distribution and is 0 for standard normal distribution [36]. Mishra et al. suggested that skewness value between +1 and -1 can be used as an indicator for the normality of the data [37]. As shown in Table 6, the skewness value for both T and P is found to be within +0.39 and -0.3. It is also noted that the mean and median are approximately the same for all cases, corroborating normality of the data. Furthermore, it

has been observed that the mean value and the standard deviation do not significantly change with increased sample size. Thus, 600 samples for estimation are chosen for data analysis in this experimentation and the precision error of the pressure transducers and thermocouples are calculated to be 0.01kPa and 0.02K respectively.

Table 6 Statistical data of pressure transducer and thermocouple

Pressure

	30 second	1 minute	2 minutes
Sample size	300	600	1200
Mean, μ (kPa)	103.30	103.30	103.29
Median (kPa)	103.30	103.30	103.29
Standard Deviation, σ (kPa)	0.01	0.01	0.01
Skewness	0.33	0.37	0.39

Temperature

	30 second	1 minute	2 minutes
Sample size	300	600	1200
Mean, μ (kPa)	291.53	291.52	291.51
Median (kPa)	291.53	291.52	291.51
Standard Deviation, σ (kPa)	0.02	0.02	0.02
Skewness	0.35	0.13	-0.30

Based on the above experiments, the root mean square error (RMSE) is calculated for each sensor:

$$\text{RMSE} = \pm\sqrt{(\text{Accuracy error})^2 + (\text{Precision error})^2} \qquad (2)$$

As the sensors are proven to be precise, the errors are seen to be dominated by the effect of the accuracy of the sensors. Thus, the total uncertainty error, using Eq. 2, is deduced to be:

$$\text{Measured pressure reading} = \text{True Value} \pm 0.6 \text{ kPa} \qquad (3)$$

$$\text{Measured temperature reading} = \text{True Value} \pm 0.38 \text{ K} \qquad (4)$$

4.3 Error Propagation to Mass Flow

Figure 7 shows the instrumentation for flow measurement. Mass flow was calculated as a product of the density (ρ), area (A) and velocity (v):

$$\dot{m} = \rho A v \qquad (5)$$

A pressure transducer was installed on the duct wall and a thermocouple inserted into the duct was used to measure to measure the static pressure (P_s) and temperature (T) of the flow. These measurements were used to calculate the density:

$$\rho = \frac{P_s}{RT} \qquad (6)$$

where R is the universal gas constant, 287.05 JK/kg.

The velocity of the flow could not be measured directly. Thus, a total pressure probe was manufactured and installed facing the direction of the flow; the pressure transducer was mounted at the tip to measure the total pressure (P_t) of the flow. The measured P_t and P_s was used to calculate the dynamic pressure (P_d):

$$P_d = P_t - P_s \qquad (7)$$

Subsequently the velocity was calculated as a function of P_d and ρ:
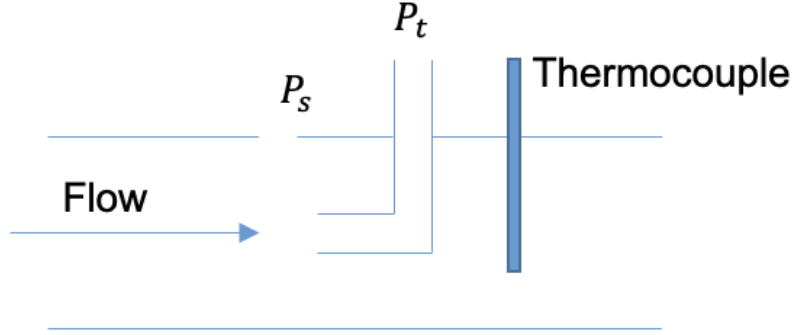
$$v = \sqrt{\frac{2P_d}{\rho}} \qquad (8)$$

Figure 7: Instrumentation for mass flow measurement

The steps for mass flow error calculation are adopted based on the method described in [38]. The maximum accuracy error observed in testing of pressure transducer (±0.6kPa) and thermocouple (±0.38K) are used to calculate the maximum error propagation to mass flow. First, the error propagation to P_d from the P_t and P_s measurements is calculated.

$$\delta P_d = \sqrt{\delta P_t{}^2 + \delta P_s{}^2} \tag{9}$$

Similarly, the error propagation to density ρ is calculated as,

$$\delta \rho = \rho \sqrt{\left(\frac{\delta P_s}{P_s}\right)^2 + \left(\frac{\delta T}{T}\right)^2} \tag{10}$$

Subsequently the error propagation to velocity is calculated using,

$$\delta v = v \sqrt{\left(\frac{\delta P_d}{P_d}\right)^2 + \left(\frac{\delta \rho}{\rho}\right)^2} \tag{11}$$

Finally, the error propagation to mass flow is calculated:

$$\delta \dot{m} = \dot{m} \sqrt{\left(\frac{\delta \rho}{\rho}\right)^2 + \left(\frac{\delta v}{v}\right)^2 + \left(\frac{\delta A}{A}\right)^2} \tag{12}$$

24

Using the above-mentioned equations, the error propagation to mass flow for the experimental data is reported in Sections 5 and 6.

5 GTF Experimental Validation

In this section the validity of the T, P and ṁ data collected from the GTF is presented. To do this, the first step is to conduct a sensor continuity check which helps to identify the installed sensor locations throughout the PACK that successfully generate data. Subsequently, the measurements acquired in terms of T and P under various ambient conditions are presented and discussed based on first principles and best engineering knowledge of the PACK operation. This is done with the aim of verifying the repeatability of the GTF for producing the PACK T and P data. Following that, based on the acquired T and P (static and total) measurements, the derived mass flow values at various locations of the PACK are discussed. Finally, the overall acquired data in terms of the T, P and ṁ, under various PACK operating modes including the effect of the trim system, is presented and discussed in order to verify the consistency of the data generation.

5.1 Sensor Continuity Check

Table 7 provides an overview of the installed sensor locations throughout the PACK. These locations are consistent with the stations illustrated in Figure 1. The table shows the working status of the installed sensors for data collection. Since the scope of this paper is limited to verification of SESAC in terms of T, P and ṁ, the discussion on the RH and valve angle sensors is omitted, and only the sensors related to the measurements of T, P and ṁ are discussed. The sensor continuity checks were first performed under ambient conditions, while keeping the PACK switched off, and were found to be successfully generating data. However, upon running the PACK, it was discovered that the PT1, PT4, PT5, PT6 and PT7 sensors as illustrated in Table 7 were providing misleading data. At PT1 the total pressure probe was broken when fitting the PACK into the aircraft and could not be replaced due to limited access. With regards to PT4, PT5, PT6 and PT7 sensors, these represent ram total pressure sensors, and they failed to provide usable data due to the positioning of their respective pitot-static tubes within the ram duct. Therefore, the data acquired from these sensors was excluded from the

analysis. Since the data measurements failed at these locations, alternative engineering based approaches were devised in order to determine the mass flow at target locations, and are outlined in Section 5.3.

Table 7 Sensor working status

Sensor Location	Temperature	Static Pressure	Humidity	Valve Angle	Total Pressure
Core					
PV_i	T1	P1			Pt1
pTCV	T2	P2			Pt2
$PHX_{h,o}$	T3	P3			
CMP_o	T4	P4			Pt3
$SHX_{h,o}$	T5		RH1		
$RHX_{h,o}$	T6	P6			
$CHX_{h,o}$	T7	P7	RH2		
$RHX_{c,i}$	T8	P8	RH3		
$RHX_{c,o}$	T9	P9	RH4		
TRB_o					
$CHX_{c,i}$	T10	P10	RH5		
$PACK_o$	T11	P11	RH6		
Cold Side (RAM)					
$PHX_{c,i}$	T12	P12			Pt4
$PHX_{c,o}$	T13	P13			Pt5
$SHX_{c,i}$	T14	P14			Pt6
$SHX_{c,o}$	T15	P15			Pt7
Valve					
PV				V1	
TCV-Pri				V2	
TCV-Sec				V3	

Legend	
	Successfully acquired data
	Broken
	Unable to generate useful data
	Out of scope of this paper

5.2 Temperature and Pressure Measurements

Having successfully completed the continuity checks on the sensors, the next step is to generate T and P data throughout the PACK under different ambient conditions while operating the PACK under constant cabin demand. This process will provide data that can be used to assess the repeatability of T and P data acquisition using the GTF. Reference cases RC1, RC2 and RC3 were selected from Table 3 as they all represent cabin demand of 24ºC with the trim system on, under varying ambient condition.

Figure 8 (a) and (b) present the acquired T and P data for the selected RCs. Note that as determined in Section 4.2, the measured T and P values have an uncertainly of ±0.38K and ±0.6 kPa respectively. The error bars could not be incorporated in Figure 8 due to the relatively small variation in uncertainty relative to the scale of the measurement. Referring to Figure 8(b), the station pTCV represents the PV outlet condition, where a pressure drop is apparent with respect to the station PV inlet (PV_i). This pressure drop across the PV occurs due to the pressure losses associated with the installed butterfly valve. In Figure 8(a), a small temperature drop of approximately 4K is also noticed across the PV, which can be attributed to heat loss to the ambient air.

Analysing both T and P downstream of the pTCV location, the flow travels through the core section of the PACK (see Figure 1). Immediately downstream of the pTCV is the PHX, which uses the ram air as a heat sink to significantly drop the temperature of the bleed air. As shown in Figure 8(b), a small pressure drop across the PHX is observed which is due to the inherent pressure losses associated with the PHX. After the PHX the air undergoes compression in the ACM compressor which increases both the temperature and pressure of the air as seen at location CMP_o in Figure 8. Post compression, a temperature drop at the $SHX_{h,o}$ is observed in which the SHX removes most of the heat added due to compression. Beyond this stage, humidity is removed from the air in the HPWS, which is composed of a series of heat exchangers acting as a reheater and a condenser. As expected, as the air passes through these heat exchangers, the temperature varies marginally to allow condensation and water extraction and the pressure drop occurs due to the inherent pressure losses associated with the heat exchangers. Once the air has humidity removed, it is supplied to the turbine for expansion.

Due to the turbine expansion, both the pressure and the temperature of the air drop substantially. In Figure 8(b), the effect of the pressure drop due to expansion across the turbine can be seen at the Merge_o location. The turbine outlet temperature can often reach below freezing, which wasn't captured in the data as it was not possible to install a thermocouple directly after the turbine outlet due to space limitation. At this point, the hot bleed flow from the TCV-Pri is mixed at the merge component placed immediately downstream of the turbine in order to prevent ice formation and match the demanded temperature. The aircraft utilises a factory-installed thermal sensor at WS_o, which dictates the opening and closing of the TCV in order to match the demanded temperature. This broadly explains the behaviour of the T and P across each component as the bleed air goes through the PACK.

The overall variation observed in the RCs presented in Figure 8 can be attributed to multiple factors such as:

1. The APU provides the bleed air which according to the maintenance manual [22] vary with respect to the ambient condition.
2. As the experiments were performed on different days, the cabin temperature across different cabin zones cannot be practically maintained at a constant temperature. This affects the temperature control loop of the PACK-zone controller, which consequently has an impact on how the flow control valves such as the TCV and trim are regulated in order to deliver the demanded cabin temperature.
3. The variation in pressure across the ACM (CMP_o through to $\text{RHX}_{c,o}$) can be attributed to the differences in the mass flow through the core, regulated by the PACK zone controller through the trim system mass flow extraction.
4. The variation observed in the temperature profile, see Figure 8(a), are found to prominent across the HPWS (from $\text{SHX}_{h,o}$ through to $\text{RHX}_{c,o}$). As the function of the HPWS is to regulate humidity and extract excess water content from the air, the variation in temperature can be sensitive to the RH in the bleed air on the test day [15].

5. At the WS_o station the temperature should match the demanded temperature according to the AMM, this is not found to be the true in all cases. The exact reason why the PACK is not able to match the demanded temperature at WS_o cannot be pointed out due to the inherent highly integrated nature of the PACK with the upstream bleed and the downstream air distribution and trim system, as well as the intervention of the PACK zone controller on the overall system.

Considering the aforementioned limitation associated with the experimental testing on an actual aircraft, it can be safely said that the developed GTF is capable of producing data for temperature and pressure which is found to be repeatable in terms of the trend. This is in the sense that the acquired data is coherent in terms of representing the physics of the PACK components. The acquired data shown in Figure 8 is logical in terms of capturing the components functional outputs, and that it follows the physics first principles of the system. However, the engineering aspect of the data cannot be repeatedly reproduced due to the limitation associated with the lack of knowledge and control over the other sub-system i.e., bleed air, air distribution, trim system, and the PACK control system. For example, without any insight of the employed PACK zone control logic, it is not possible to reason why the WS_o temperature can't be matched against the demanded temperature. Furthermore, the RC2 pressure rise across the compressor is significantly lower relative to the RC1 and RC3, this is due to the fact that for RC2 the trim system extracts higher mass flow, resulting in reduction in the core mass flow which consequently affects the operating point of the ACM for RC2. Without any detailed insights of the control logic employed for the control of the trim system the engineering reason for why the trim system decided to extract more mass flow for RC2 relative to RC1 and RC3 cannot be systematically comprehended.
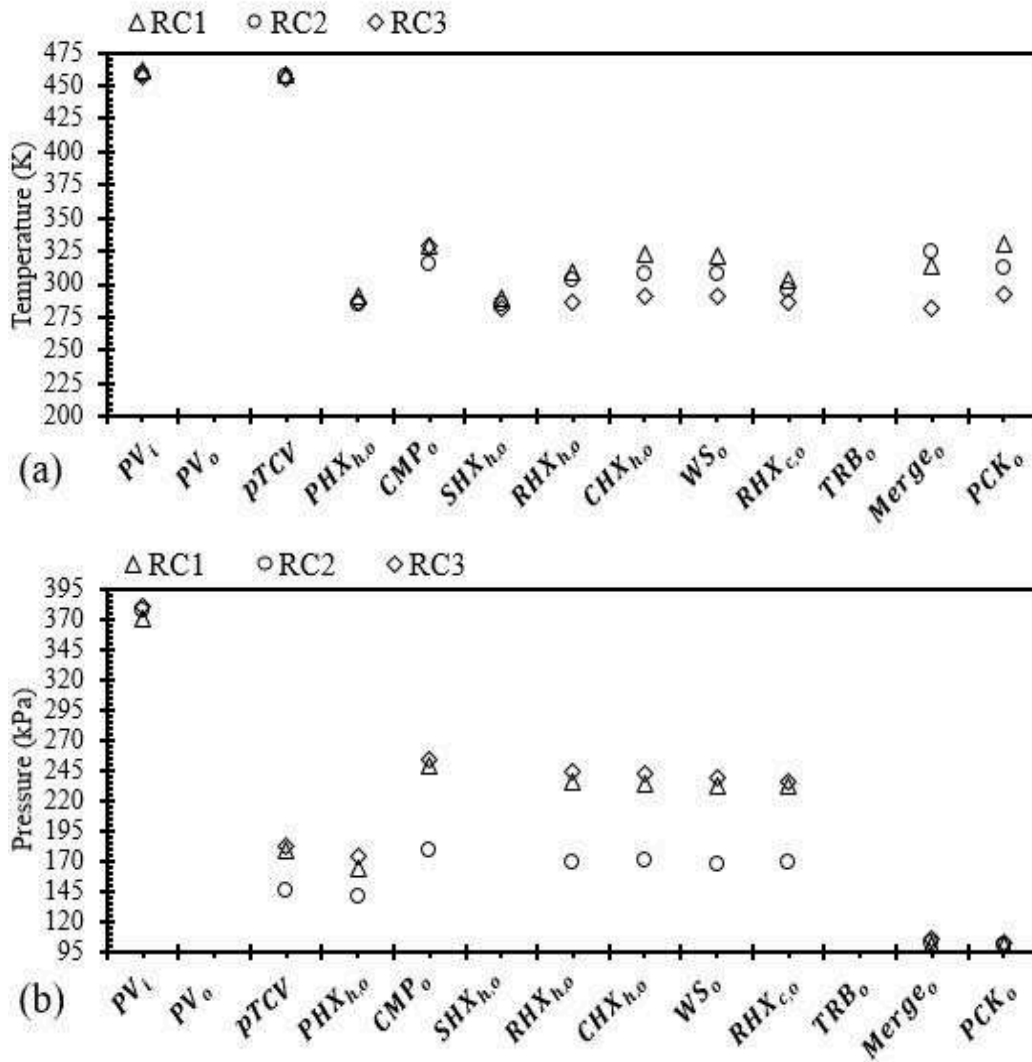
.

Figure 8 GTF repeatability test data, (a) Temperature, (b) Pressure.

5.3 Mass Flow Measurements

Mass flow measurements were attempted at four locations throughout the PACK: (i) PV_i, (ii) pTCV, (iii) CMP_o, and (iv) ram. Out of the four, successful measurements were attained at only two locations: (i) pTCV and (ii) CMP_o.

With regards to the ram mass flow, the total pressure transducers installed at the PHX and SHX ram inlet generated unusable data, and instead, the measured temperature readings across the PHX and SHX, and the measured CMP_o mass flow values were used to determine the ram mass flow. This was based on an energy balance

matching the heat picked up by the ram flow against the heat absorbed by the flow through the heat exchanger:

$$\dot{m}_{RAM} = \frac{\dot{m}_{CMP,o} * c_p * (T_{PHX,ho} - T_{PHX,hi})}{c_p * (T_{PHX,ci} - T_{PHX,co})} \qquad (13)$$

The pitot-tube intended to measure PV_i was found to be broken, when the PACK was installed back into the aircraft, and an alternative approach was taken to determine the PACK inlet mass flow. Upon switching on the PACK under a given cabin temperature demand, the PV opens, and flow enters the system. As stated in Section 2.1, there exists a control loop that regulates the opening of the TCV-Pri valve based on the WS_o temperature sensor feedback. At the beginning of the PACK start-up sequence, the WS_o temperature sensor will not immediately see a rise in temperature, and hence the PACK controller (due to lag) will not respond. Therefore, the TCV remains spring loaded closed and will only open once the initial control loop between the PACK controller and the WS_o sensor is completed [21].

Figure 9(a) illustrates a simplified view of the station sequence from PV_i through to CMP_o, and highlights the location of the pressure transducers and thermocouples installed for supporting the mass flow measurement. A mass flow reading is taken at the pTCV location immediately downstream of the TCV_pri bypass, and at CMP_o. Therefore, engineering judgement would suggest that, for PACK operating conditions under which the TCV_pri bypass valve is closed (e.g. during initial phase of the PACK start-up), the mass flow measured at pTCV would represent the mass flow through the PV. This is because the PV regulates a near constant mass flow for any given ambient condition [22].

As shown in Figure 9(b), when the PACK is switched on, the measured pTCV mass flow peaks and then gradually reduces. From the preceding discussion, the peak is due to the TCV-Pri being closed and all the bleed mass flow fed through the pTCV station. Once the WS_o sensor completes the initial feedback loop with the PACK controller, the TCV-Pri opens and part of the mass flow is fed through the TCV stream, accounting for the drop in pTCV mass flow and the approach to steady state, around 10 seconds after

the start. The mass flow characteristics presented in Figure 9 are found to be consistent for all the RCs presented in Table 3.
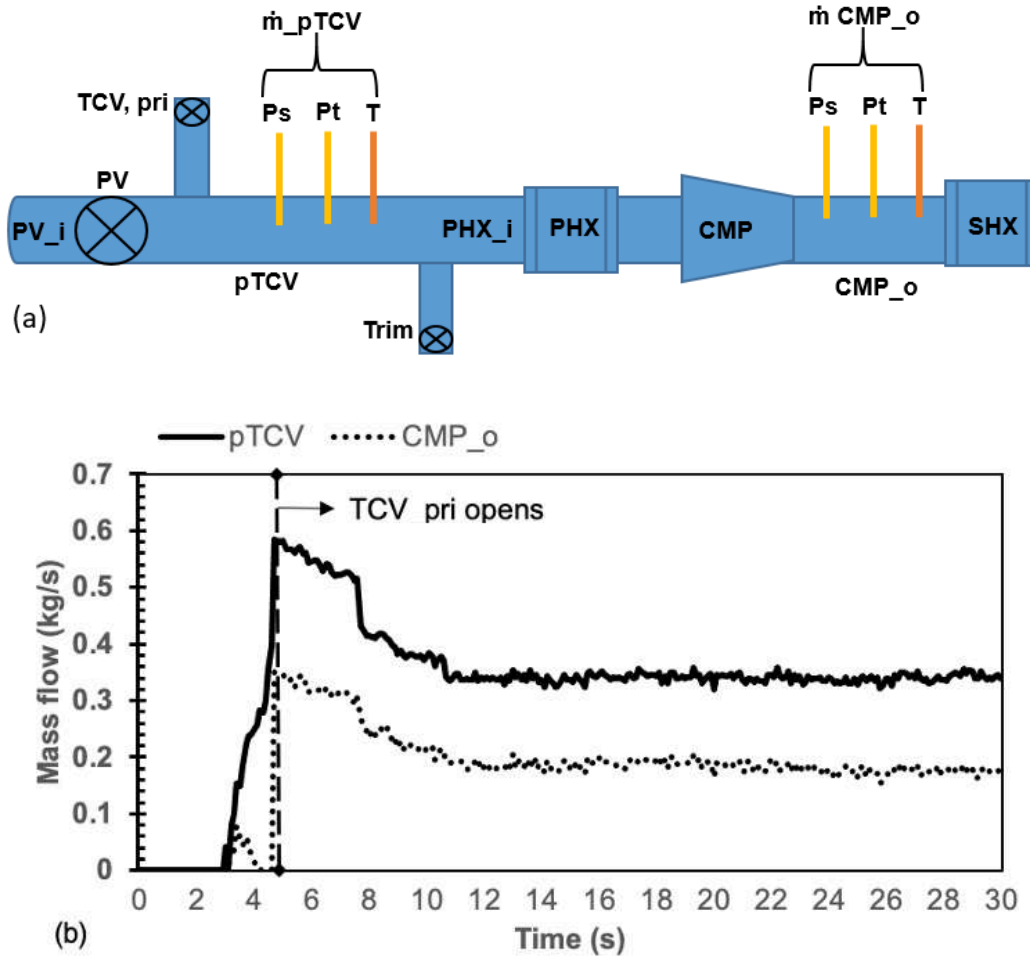

Figure 9: (a) Simplified schematic for mass flow measurements, (b) Measured mass flow as a function of test time at pTCV and CMP_o stations, 0 = PACK off.

Based on the above engineering judgement it was assumed that the mass flow peak observed at pTCV provides a good estimation of the mass flow at PV_i. The measured initial peak mass flow values at pTCV, as well as the corresponding steady state values for pTCV, and CMP_o, for RC1, RC2 and RC3, are presented in Table 8. Also presented are the derived ram mass flow values based on the energy balance equation (Eq. 13). The TCV-Pri mass flow is derived using:

$$\dot{m}_{TCV-Pri} = \dot{m}_{initial\ peak\ at\ pTCV} - \dot{m}_{pTCV} \tag{14}$$

In Figure 9(b), it is seen that the measured CMP_o mass flow reaches a peak and then gradually drops due to the opening of the trim valve before reaching a steady state. As the trim valve is placed between the pTCV and CMP_o location, the trim mass flow is derived as the difference between these two measured mass flows:

$$\dot{m}_{Trim} = \dot{m}_{pTCV} - \dot{m}_{CMP\_o} \tag{15}$$

Note that all three cases presented in Table 8. were tested on three different days under same PACK demand of 24C. The ambient conditions are 11.5°C, 9°C and 5.5°C respectively for RC1, RC2 and RC3. Starting from the initial peak measured at the pTCV which represents the bleed flow through the PV ($\mathbf{PV_i}$ mass flow), it can be seen that the PV inlet mass flow increases with increase in ambient temperature, this is found to be consistent with the performance characteristics of the APU prescribed in the AMM [22]. With regards to the ram mass flow, as per the AMM [22], during ground operations the ram door is fully open in order to allow maximum mass flow to flow through the PHX and SHX. The acquired ram mass flow values remain consistent across all three cases.

The TCV and trim mass flows are regulated by the PACK zone controller based on the thermal sensors installed at the PACK, mixing manifold and cabin. The data suggests that relative to the inlet mass flow the controller extracts 24%, 50%, and 30% of the mass flow and bypasses it through the trim system for RC1, RC2, and RC3 respectively. The controller characteristics for RC1 and RC3 concur reasonably, however, the extraction of as much as 50% of inlet mass flow for RC2 is peculiar specifically when considering the fact that in all three cases the PACK demand is maintained constant. Such behaviour of the control system cannot be explained without detailed knowledge of the employed control logic. The acquired pressure data, as shown in Figure 8 for all three RCs is consistent with the mass flow data shown in Table 8. RC1 with highest mass flow through the core corresponds to higher pressure rise across the compressor and likewise for RC2 with lowest mass flow through the core corresponds to lowest pressure rise across the compressor. It is clear that both the TCV and trim mass flow have a direct impact on the mass flow through the core of the PACK and therefore on the performance

characteristics of the core components i.e. PHX, SHX, ACM, HPWS. It can therefore be safely claimed that the developed GTF supports the acquisition of T, P and $\dot{m}$ data that obeys the physics first principles of the PACK system components operating under different ambient conditions. The engineering aspect of the PACK i.e. the controller characteristics cannot be adequately reproduced due to lack of access to the employed control logic and the characteristics of the downstream systems i.e. mixing manifold, air distribution, trim system.

Table 8 Measured and derived mass flows (kg/s) for RC1, RC2 and RC3.

Reference cases	Initial peak measured at pTCV	TCV-Pri (derived)	pTCV (measured)	Trim (derived)	CMP_o (measured)	Ram (derived)
RC1	0.680	0.175	0.505	0.163	0.342	0.693
RC2	0.615	0.062	0.553	0.321	0.232	0.691
RC3	0.585	0.065	0.520	0.180	0.340	0.695

5.4 Consistency Test

Having demonstrated that the GTF can generate T, P and $\dot{m}$ data throughout the PACK under different ambient conditions, the next step is to analyse the GTF's capability to capture the PACK performance characteristics under different operating modes, i.e. hot and cold cabin demand with trim system on and off, as given in Section 3.2 To do this, the RCs selected for the demonstration of this activity are: (i) RC3 (hot demand–trim on), (ii) RC4 (cold demand-trim on), (iii) RC5 (cold demand-trim off), and (iV) RC7 (hot demand-trim off). Note that hot and cold refer to cabin temperature demands of 24°C and 18°C respectively (Table 3). Figure 10 and Table 9 represent the acquired T, P and $\dot{m}$ data for the selected RCs. The overall analysis of the acquired data is presented in two parts, first the corroboration for the PACK hot and cold operation with trim system off (RC5 and RC7) is presented, and then the discussion with regards to (RC3 and RC4) the effect of trim system being on and off under hot and cold demand is given.

In terms of the PACK hot and cold demand with trim off operation, it is expected that under the cold demand operation, the ACM must be operated as such that it provides maximum expansion in order to attain maximum cooling through the turbine. For a given cold demand operating condition this can be accomplished by minimising the bypass flow through the TCV and trim, and allowing maximum mass flow to flow through the core of the PACK in order to maximise turbine expansion. Likewise, under the hot demand operating condition, it would be favourable to minimise the expansion through the turbine by allowing minimum mass flow to flow through core.

The acquired results for mass flow under cold demand and hot demand with trim system off are presented in Table 9. First, as the RC5 and RC7 cases corresponds to the trim off condition there is no flow expected to flow through the trim valve. As shown in Table 9, the trim mass flow value for RC5 is 0.044kg/s and for RC7 is 0.01kg/s, derived using Eq.15. The respective values for the trim flow are attributed due to the presence of uncertainty associated with the measured T and P values and its propagation to mass flow measurements at pTCV and CMP_o as explained in Section 4.3. The corresponding uncertainty values for pTCV and CMP_o mass flows are tabulated in Table 9, and the resultant uncertainty propagated to the trim mass flow is calculated using:

$$\delta\dot{m}_{Trim} = \sqrt{\delta\dot{m}_{pTCV}^2 + \delta\dot{m}_{CMP\_o}^2} \tag{16}$$

This gives trim mass flow uncertainty values of ±0.117 and ±0.122kg/s for RC5 and RC7 respectively. These uncertainty values clearly bound the trim flows given in Table 9 and explain their near zero values in terms of experimental uncertainty.

With regards to the TCV flow, it would be expected that the PACK controller must bypass lower mass flow through the TCV for RC5 relative to RC7. RC5 have a 19% lower mass flow through the TCV and with trim system off, this leads to 28% higher mass flow through the core for RC5 relative to RC7. With higher mass flow through the core, a higher expansion through the turbine is attained, which translates to more power being transferred to the compressor relative to the RC7. As a result, both the T and P at the compressor outlet are found to be higher relative to the hot demand cases, shown in Figure 10(a) and (b).

Note that at the stations $PHX_{h,o}$ and $SHX_{h,o}$ of Figure 10(a), the temperature drop is marginally less in the cold temperature demand cases. The cold ram mass flow through the PHX and SHX remains constant throughout all four cases. However, the increase in the core mass flow (i.e. hot mass flow for PHX) has an effect on the heat transfer through the PHX and SHX, following Eq.13. Downstream of the SHX, humidity is removed from the air in the HPWS components. Discussion of humidity is not within the scope of this work and so will be omitted.

As discussed in Section 2.2, if the trim system is switched on then the PACK-zone controller dictates the status of the trim valve based on the cabin temperature feedback and the imposed cabin demand. This has a consequent impact on the amount of mass flow that can be attained through the PACK core. RC4 presents cold cabin demand with trim system on, however, despite of trim system being on, no flow through the trim system is observed. The trim mass flow value for RC4 is derived to be 0.035kg/s and is within the uncertainty error. The likely reason why the PACk-zone controller decided to close the trim valve is to allow maximum mass flow to flow through the core in order to maximise expansion through the turbine as desired in order to adhere with the cold demand. Therefore, the observed PACK performance characteristics for RC4 coincide closely with RC5 under which the trim system is kept off, Figure 10(a) and (b) show that the T and P profile for these 2 cases are almost identical. Furthermore, it can also be observed that the pressure rise across the compressor is significantly higher for both of these cases, allowing maximum expansion through the turbine.

With regards to the hot (24°C) cabin demand case with trim system on (RC3), the PACK-zone controller opens the trim valve and maintains flow through the trim system. This consequently reduces the overall flow through the core of the PACK, as not as much cool air needs to be generated through the ACM as in the previous cases discussed. The only distinction between the hot cases (RC3 and RC7) with trim system on and off is that in the latter case, due to closure of the trim system, the hot bleed air is bypassed using the TCV stream instead of the trim system, see Figure **9**(a). It is to be noted that the experimental investigation is only focussed on the PACK and at this stage the trim and TCV control logic is not known. As shown in Table 9, the mass flow through the TCV for

RC7 is significantly higher (0.265) relative to RC3 with trim system on (0.065). In both cases, ultimately, the flow through the PACK core is reduced in order to limit any unwanted cooling through the ACM, allowing the PACK to comply with the imposed hot cabin demand. The uncertainty error in Table 9 is estimated using:

$$\delta \dot{m}_{TCV\_pri} = \sqrt{\delta \dot{m}_{intial\ peak\ at\ pTCV}^2 + \delta \dot{m}_{pTCV}^2} \tag{17}$$
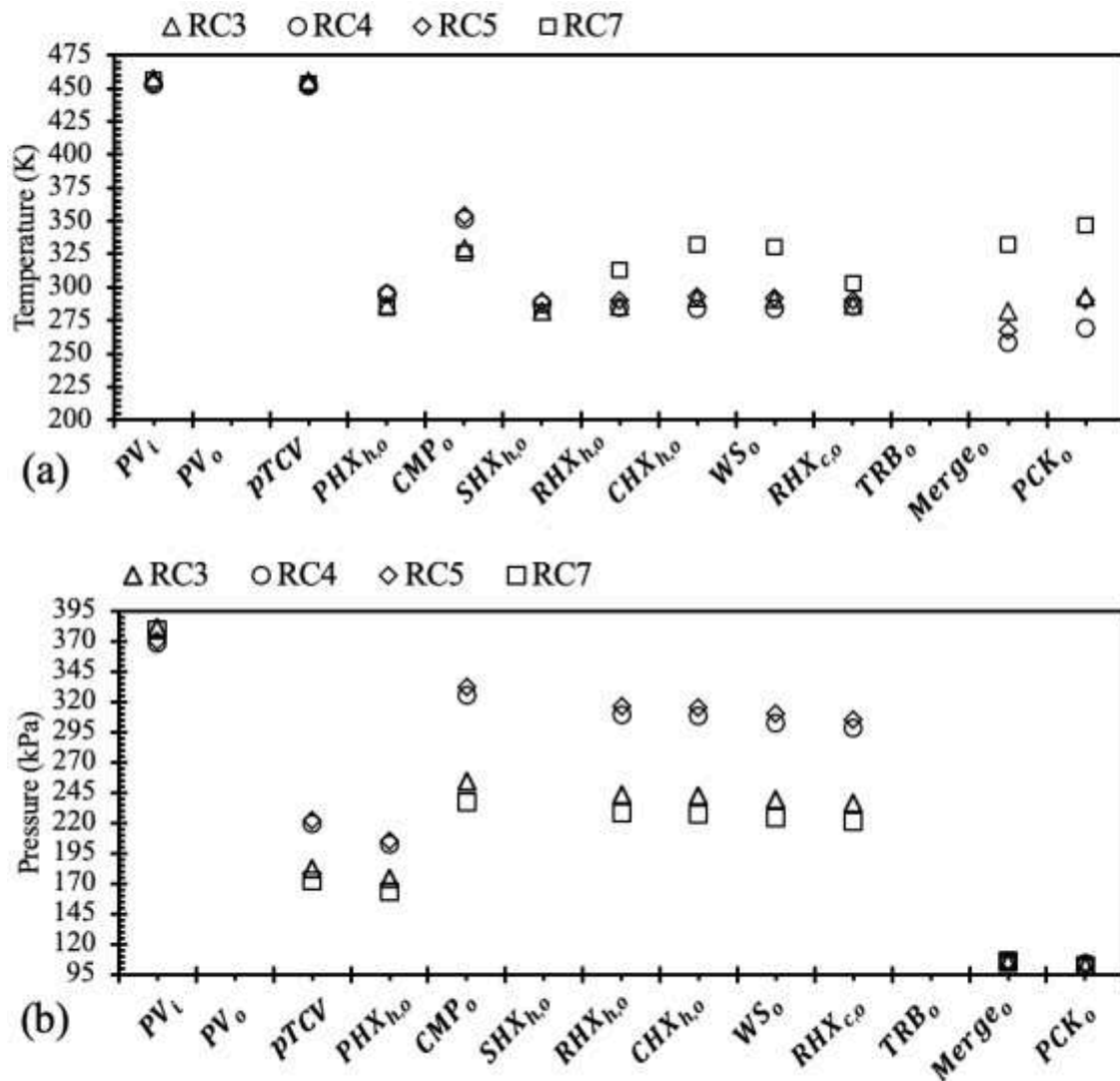

Figure 10 (a) Temperature profile and (b) Pressure profile, for selected reference

Table 9 Mass flow (kg/s) variation for reference cases with different cabin demand and trim flow status

Reference cases	Cabin demand	Trim Status	TCV-Pri (derived)	$\delta\dot{m}$, TCV-Pri	CMP_o (measured)	$\delta\dot{m}$, CMP_o	Trim (derived)	$\delta\dot{m}$, Trim
RC3	H	On	0.065	±0.095	0.340	±0.054	0.180	±0.089
RC4	C	On	0.222	±0.128	0.405	±0.055	0.035	±0.114
RC5	C	Off	0.222	±0.129	0.396	±0.057	0.044	±0.117
RC7	H	Off	0.265	±0.125	0.310	±0.056	0.010	±0.122

The GTF have captured the performance characteristics of the PACK under hot and cold demand consistently. The acquired data suggest that under cold demand PACK operation, irrespective of the status of the trim system (on or off), the PACK controller permits maximum mass flow to flow through the core of the PACK in order to maximise the expansion through the turbine. The PACK is found to be operating at 28% higher core mass flow under cold demand compared to the hot demand cases. Based on the acquired data, it can be safely said that under PACK cold demand operation the trim system can be maintained off, as the PACK-zone controller dictates the status of the trim flow, which is found to be same under trim off and trim on condition. With regards to the hot demand PACK operation the data suggest that the PACK-zone controller choses to bypass maximum hot mass flow through the trim system in case if the trim system is on. And in case if the trim system is off, the controller instead uses the TCV to bypass the hot mass flow, in both cases however, the core mass flow is ultimately minimised so that the undesired expansion through the turbine can be maintained minimum.

In terms of capturing the data consistently, the only short fall that can be observed from the data is associated with the WS_o outlet temperature, this temperature is expected to be matched against the imposed demanded temperature as per the AMM [22]. As elaborated in the preceding section, the reasoning for why the PACK controller is unable to match the WS_o temperature against the demanded temperature cannot be

comprehended due to lack of access to the employed PACK zone control logic for regulating the WS_o temperature as well as the lack of the performance characteristic of the downstream systems i.e. mixing manifold, air distribution and trim system. Apart from the regulation of the WS_o temperature, the GTF consistently captures the performance characteristics of the PACK components and are found to obey the first principles of the components physics. Furthermore, the data is also able to capture consistently the engineering aspect of the PACK operation in terms of the regulation of the trim system. The acquired data from the consistency test can be used to compare estimations of a physics first principles based simulation model i.e. SESAC to verify its capability to produce the performance characteristics under various PACK operating conditions.

6 Comparison of SESAC Against the SESAC Simulation

Having successfully demonstrated the capability of the GTF to capture the PACK performance characteristics in terms of T, P and $\dot{m}$ under different ambient and operating conditions, in this section the estimation acquired from a simulation model based on the first principles of the components physics are compared against the data acquired through the GTF. The SESAC simulation framework discussed under Section 2.3 has been used to develop a reference simulation model for the B737-400 PACK. All the RCs have been simulated and compared against data and RC4, RC5, RC6 and RC7 are selected for demonstration purposes, as these RCs represent the PACK operation under hot and cold demand with trim system on and off and are deemed suitable to test and demonstrate SESAC's capability. First, the employed simulation model and the corresponding boundary conditions for the selected RCs are presented and discussed. Subsequently the overall average relative difference between the test data and simulation is discussed for the selected RCs. Finally, the T, P and $\dot{m}$ test data is corroborated against the simulation at PACK component level.

6.1 Reference SESAC Simulation Model

The theoretical and computational development of the SESAC PACK simulation model for a B737-800 has been reported [16], [17]. For the implementation of simulation in this

paper, the reported model has been reproduced and is implemented with some modifications in order to represent the B737-400 PACK simulation. The developed B737-400 PACK model is presented in Figure 11. In terms of the modifications, a dedicated integral controller has been incorporated to account for the effect of the trim system [21], detailed in Section 2.2. The rest of the model configuration remains identical to the adopted reference model, elaborated in Section 2.3.
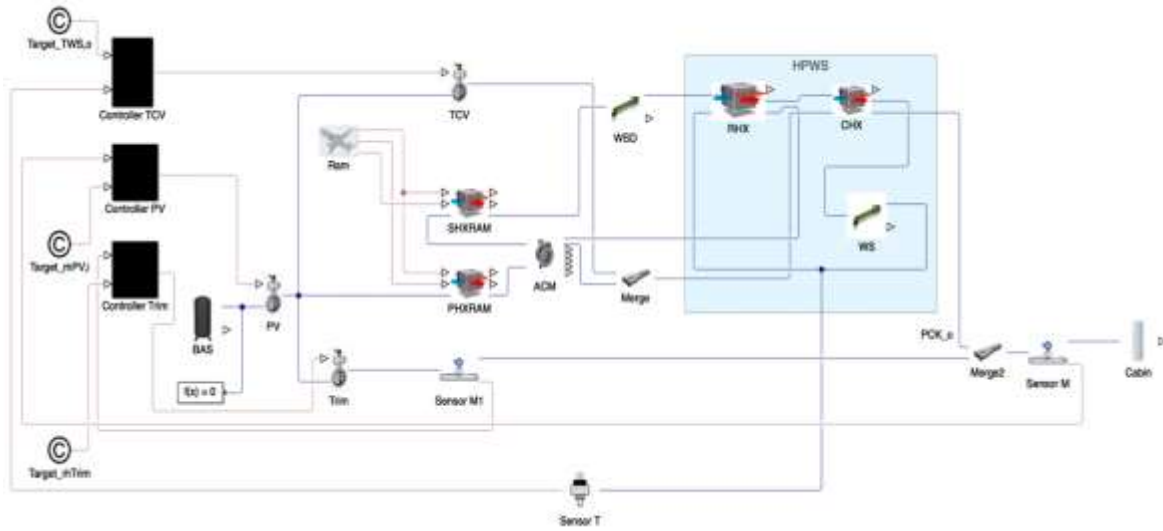

Figure 11 Simulation model of the B737-400.

In order to implement the developed simulation model for the selected RCs, boundary conditions must be defined. The overall required boundary conditions for the model simulation can be categorised in five parts, as shown in Table 10. As all the experimental testing was conducted at sea level static conditions, the aircraft state conditions were set to ground operations. The measured ambient condition, and the ram mass flow derived using energy balance equation as outlined in Section 5.3, were defined in the model accordingly for each RC. The bleed air properties (T and P) were taken from the acquired experimental data. The humidity and water content were set to 0, as analysis of the humidity is excluded from this study. To meet the cabin demand, the target temperature was set as the measured WS_o temperature as prescribed in the AMM for the B737-400 PACK architecture [21]. The target mass flow was set as the measured peak value obtained from the pTCV station, which is treated as the inferred PV_i mass flow, as explained in Section 5.3. Finally, the trim mass flow derived using Eq. 16 is set as a trim

flow in the model for each RC. All SESAC simulation were performed with the assumption that the components are free from degradation. Therefore, the degradation severity level for each component was set to 0.

Table 10 SESAC PACK simulation model boundary conditions

	Parameters	Description	Units
Aircraft State condition	Selector (S)	0 (Ground operations)	[-]
Ram (0: Ground Static)	$\dot{m}_{Ram}$	Heat-exchanger cold mass flow	[kg/s]
	T_{amb}	Ambient temperature	[K]
Ram (1: In flight)	Alt	Altitude	[m]
	Mach	Mach number	[-]
	Area	Ram door opening area	[m^2]
	%Open	Ram door percentage open	[%]
Bleed Air properties	PV_i - T	Bleed temperature	[K]
	PV_i - P	Bleed pressure	[Pa]
	PV_i - RH	Bleed humidity	[kg/k]
	PV_i - CO	Bleed water content	[kg/k]
Target Conditions	PCK_o - P	PACK outlet pressure	[Pa]
	WS_o - T	Cabin demand/ WS outlet temperature	[K]
	PV_i - $\dot{m}$	Bleed mass flow	[kg/s]
	$\dot{m}_{Trim}$	Trim mass flow	[kg/s]

One important aspect with regards to the simulation worthy of noting at this stage is that, as explained in Section 5.3, the PV_i mass flow is inferred based on the peak value measured at the pTCV, therefore any uncertainty associated with the mass flow needs to be accounted for prior to incorporating it in the model as a boundary condition. The method detailed in Section 4.3 for uncertainty propagation to mass flow calculation was adopted to determine the estimates for the associated uncertainty error. Figure 12(a) presents the acquired peak value at the pTCV station for RC4, RC5, RC6 and RC7 and the respective error bounds for the uncertainty. The estimated uncertainty error range is found to be high and can be attributed due to the use of multiple sensors to measure the acquired T and P for supporting the mass flow calculations. In addition, as reported by the authors in their study dedicated to the evaluation of the control system of the PACK,

it has been demonstrated that the PV maintains a near constant mass flow due to its design dependency on the pressure drop across the valve and the ambient pressure. Therefore, any sudden change in ambient pressure can impose a marginal variation in the mass flow through the PV [21]. The effect of this marginal change in PV_i can also contribute to the overall uncertainly associated with the PV_i mass flow presented in Figure 12(a) in addition to the employed instrumentation for measuring the mass flow. In a study reported by Skliros et al. [39], the measurement of bleed mass flow using the two pressure transducers in a Boeing 747 APU lead to a maximum error of around 7%. It was identified that the uncertainly error increased with a decrease in the measured mass flow. Their findings therefore suggested the use of a differential pressure transducer to improve the overall mas flow uncertainty error.

In the similar fashion to the PV_i mass flow, there is uncertainty associated with the measured ram flow. As elaborated in Section 5.3, the ram mass flow is measured based on the measurements of the temperatures across the cold and hot side of the PHX, and the measured CMP_o mass flow. The associated uncertainly with these measured quantities will propagate to the ram mass flow. Using the same method adopted for the uncertainly calculation of the PV_i, the estimate of the uncertainly error associated with the ram mass flow is calculated for all RCs and is presented in Figure 12(b).

Figure 12(a) shows the PV_i mass flow values for the simulation, labelled as PV_i (SESAC). It is evident that the PV_i values used for the simulation fall within the overall uncertainty associated with the PV_i mass flow as elaborated earlier. Figure 12(b) shows that the ram mass flow values for the simulation were incorporated without making any alterations across all cases. Therefore, from the overall boundary conditions tabulated in Table 10 only the PV_i mass flow was adjusted in order to attain a consistent match against the overall data in terms of T, P and ṁ. The pressure loss coefficients for the HXs (PHX, SHX, RHX, CHX) as well as the mechanical efficiency of the ACM, were maintained fixed throughout the simulation for all cases as reported in previous study on the B737-800 simulation[16]. Table 11 presents the incorporated boundary condition values corresponding to all RCS.
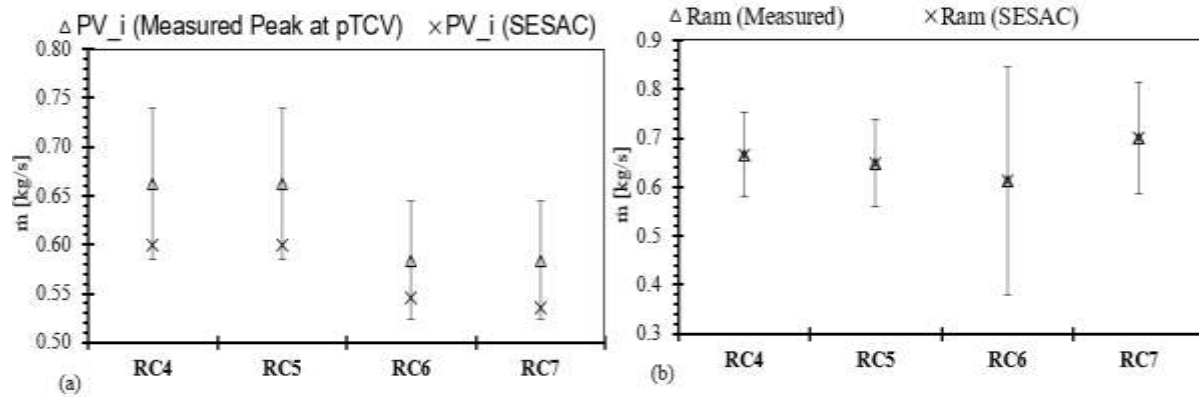
Figure 12 PV inlet mass flow uncertainty error for selected RCs

Table 11 Boundary condition for the reference cases to run simulation

Reference Cases	$PV_i – T$ (K) (measured	$PV_i – P$ (kPa) (measured)	$PV_i - \dot{m}$ (kg/s) (inferred + corrected)	$\dot{m}_{Trim}$ (kg/s) (derived)	T_{amb} (°C) (measured)	$\dot{m}_{Ram}$ (kg/s) (derived)	$WS_o – T$ (K) (measured
RC4	453.41	367.94	0.600	0.405	6.5	0.666	283.64
RC5	453.94	369.86	0.600	0.396	6.5	0.649	292.23
RC6	453.04	373.84	0.545	0.180	5.5	0.614	330.40
RC7	456.47	379.54	0.535	0.310	5.5	0.701	330.51

6.2 Simulation Average Relative Differences

Prior to proceeding with the detailed analysis of the test data against the simulation it is important to highlight that some discrepancies are inevitable between the simulation and the test data, and can be attributed due to the following reasons [16]:

1. The intrinsic wear and tear of the system. The Boeing 737 being used is a very old plane and its components are likely to be deteriorated from their new condition.
2. The RCs include PACK losses not accounted for in the SESAC, e.g. component leakages and the losses associated with the interconnecting duct sealings.

3. Lack of accurate resolution of the system component performance map characteristics incorporated in the SESAC components, i.e. compressor, turbine, heat exchangers.

4. The test data may include some level of component fouling in the HXs, or losses in the mechanical efficiency of the ACM. Such losses are extremely difficult to account for in a physics based (theoretical) simulation unless real engineering insight of the system is available. Lack of such engineering knowledge of the system leads to inevitable discrepancies when comparing the simulation predictions against the actual data [sim paper].

Due to these reasons the simulation discrepancies in this work are referred to as the difference rather than the error between the simulation and the test data. Furthermore, with regards to the mass flow data, the mass flow data is derived based on the measured T and P, and the differences in mass flow data therefore also stem from the uncertainly error propagation associated with the T and P measurement, as elaborated in Section 4.3.

The results for the simulation and the data for RC4, RC5, RC6 and RC7 in terms of the T, P and $\dot{m}$ are presented in Figure 13 and Figure 14. These cases present the PACK operation under hot and cold demand with trim system on and off. It can be seen that broadly the simulation captures the performance characteristics throughout the PACK with good agreement against the data. As observed in the results, in terms of the temperature comparison with the data the $\mathrm{Merge_o}$, and $\mathrm{PCK_o}$ present the highest discrepancies, and in terms of the pressure the highest discrepancies occur across the ACM. The areas of discrepancies between simulation and data is consistent across all cases, which indicates the underlying reasons to be the same. This implies that the overall behaviour of the simulation model against the data remains consistent under different PACK operating conditions.
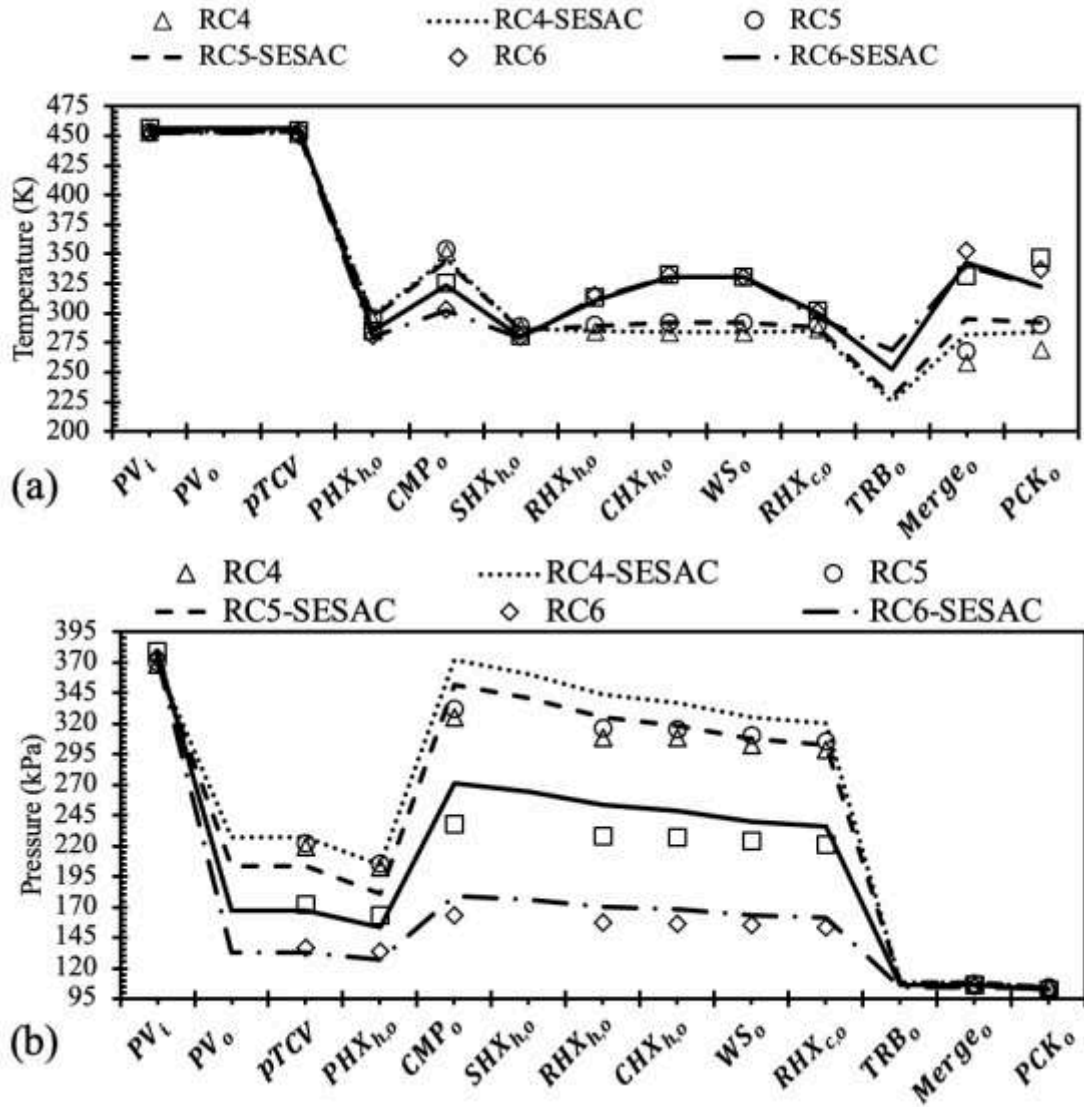
Figure 13 (a) Temperature profile and (b) Pressure profile for RC4, RC5, RC6 and RC7
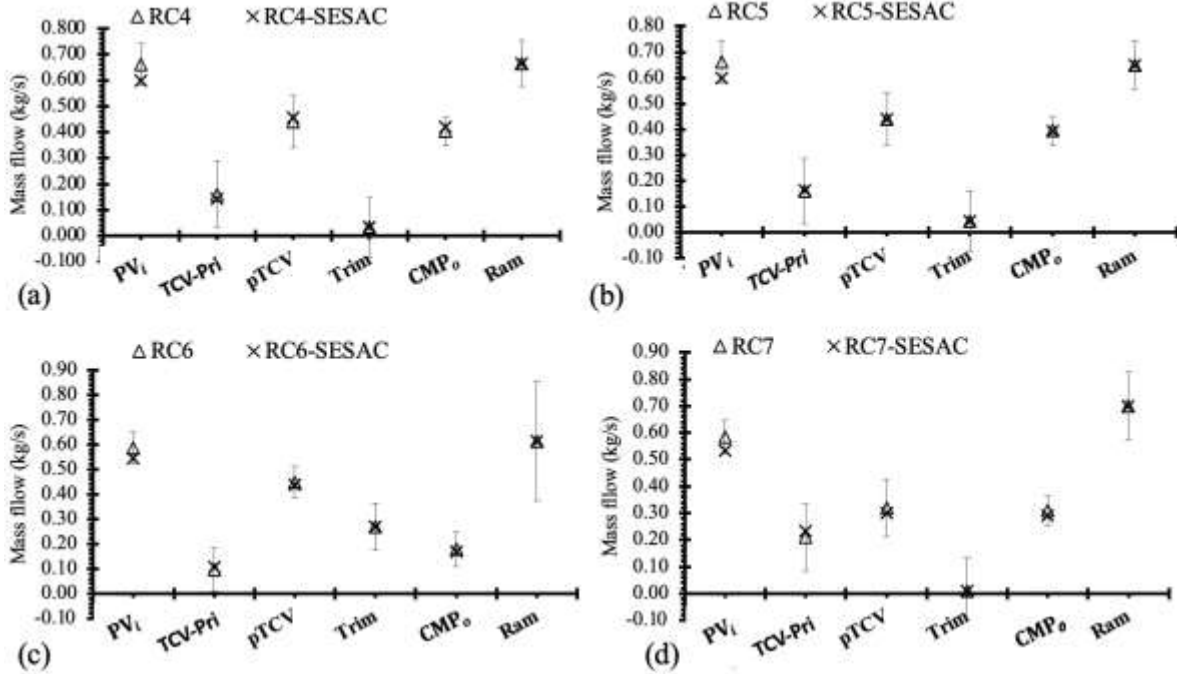
Figure 14 Mass flow measurement and simulation data for (a) RC4 (b) RC5, (c) RC6 and (d) RC7

Prior to proceeding with the analysis at the component level between the data and the simulation. it is deemed practical to first evaluate the average relative difference for T, P and $\dot{m}$. To do this, Eq.18 is applied to calculate the relative difference for T, P and $\dot{m}$ at each measurement location between the simulation and the test data throughout the PACK. The measurement locations are depicted in Figure 1. The sum of the difference for these variables is then used to calculate the average relative difference for each parameter by using Eq.19. Therefore, the average relative difference represents the overall difference between the simulation and test data with respect to T, P and $\dot{m}$ for each corresponding RC.

$$\text{Rel. Difference} = \frac{(\text{Model} - \text{actual data})}{\text{actual data}} \times 100 \ [\%] \qquad (18)$$

$$\text{Average Rel. Difference} = \frac{\sum \text{Model Rel. Diff at each station}}{\text{number of stations}} \times 100 \ [\%] \qquad (19)$$

Figure 15 presents the calculated average relative difference for all the RCs selected (RC4, RC5, RC6 and RC7). The maximum average relative difference between

the simulation and data in terms of T, P and ṁ across all RCs is found to be 2%, 8% and 6% respectively. These results show that the model can capture the overall temperature variation across the PACK with higher accuracy compared to pressure and mass flow variation. The higher model accuracy for temperature can stem from the fact that the heat exchanger effectiveness maps incorporated within SESAC are able to capture the performance characteristics of the PACK operating under ground conditions. This finding is consistent with the SESAC PACK 737-800 analysis carried out under cruise conditions [16]. With regards to the differences associated with the pressure and mass flow, these are evaluated in detail by assessing the temperature, pressure and mass flow throughout the PACK in the following section for one of the selected RCs, i.e. RC4
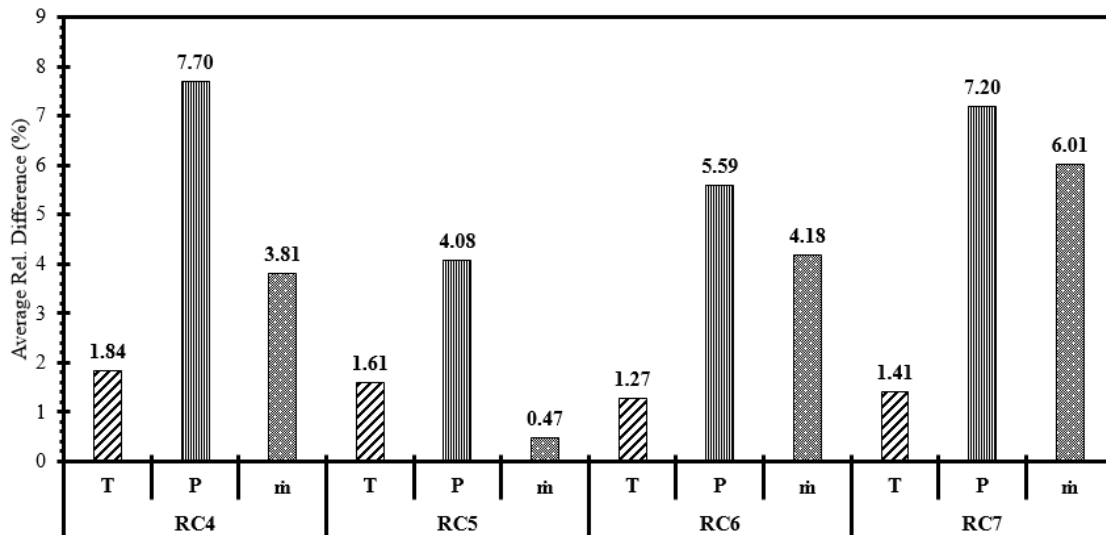
Figure 15 Average relative difference calculated for RCs with respect to T, P and ṁ

6.3 Reference Case 4 Analysis and Discussion

Figure 16 presents the results for the simulation and the test data for T, P and ṁ corresponding to RC4 at component level throughout the PACK. In order to systematically report the corroboration of the overall simulation estimates against the test data, first the situation related to the incorporation of the PV inlet and ram mass flow needs to be clarified. As explained in Section 6.1, the model requires PV inlet and ram mass flow as boundary conditions. Ram mass flow dictates the cold mass flow through the PHX and SHX, whereas the PV_i mass flow dictates how the overall energy is distributed through

the PACK core in order to condition the flow against the demanded temperature. Depending on the demanded temperature, the overall PV_i mass flow is distributed through the hot streams and cold stream of the PACK. Hot streams are represented by the TCV and trim bypass channels, whereas the flow through the core of the PACK represents the cold stream, as illustrated in Figure 1, and is responsible for the conditioning of the flow.

In order to accomplish a reasonable agreement between the simulation and the data, it is vital to match the overall distribution of the mass flow through the hot and cold streams of the PACK as well as the ram flow through the PHX and SHX. The data provides measured mass flow through the core, measurements at the CMP_o station. With regards to the flow through the hot stream, an estimation of the trim mass flow can be attained based the measured mass flow at pTCV and CMP_o station, see Eq. 16. For the purpose of simulation, an initial guess for the PV_i mass flow was made based on the inferred peak value measured at the pTCV station, and while keeping the measured ram mass flow value fixed through the PHX and SHX, the PV_i value was iteratively changed until a good match for the mass flow through the core of the PACK (at CMP_o station) was attained against the data.

Figure 16(c) shows the data and simulation mass flow values for RC4 at measured, derived and inferred stations. It is evident that the PV_i inferred value was adjusted in order to match the measured core mass flow through the PACK. The difference between the simulation and the data at CMP_o is 3.9% and falls within the uncertainly error range represented by the error bars. This was deemed as best match between the simulation and the data, as it leads to a perfect agreement for temperature throughout the core components of the PACK, as well as a reasonably acceptable match for the pressure considering the limitations associated with the resolution of the incorporated turbomachinery maps.

For the temperature profile shown in Figure 16(a), the simulation results are in good agreement with the data throughout the PACK, except the merge and PACK outlet stations. The overall average relative difference for the temperature is 1.84% and predominantly stems from the discrepancies occurring at the merge and PACK outlet stations, highlighted as dotted red circle in Figure 16(a). At the merge component (Figure

1), continuity and energy have to be satisfied. Referring to the flow through the heat exchangers and ACM as 'cold', these equations are:

$$\dot{m}_{PV\_i} = \dot{m}_{cold} + \dot{m}_{TCV\_pri} + \dot{m}_{Trim} \tag{21}$$

$$\dot{m}_{PV\_i}\,C_p T_{target} = \dot{m}_{cold} C_p T_{cold} + \dot{m}_{TCV} C_p T_{TCV} + \dot{m}_{Trim} C_p T_{Trim} \tag{22}$$

In addition, as there can be no pressure discontinuity at the merge, the pressure at the turbine outlet, the TCV outlet, and merge outlet are the same. The measured PACK outlet pressure, which is marginally lower than the merge outlet is imposed as the PACK outlet boundary condition in the model. This imposes a requirement on the turbine to produce the required expansion in order to match the downstream pressure of the data. Note that, in terms of the inlet conditions of the turbine, the temperature of the flow remains the same between the simulation and data, however the simulation has a 7.4% and 3.9% higher pressure and mass flow through the turbine relative to the data. This will inevitably result in higher expansion through the turbine, and therefore higher temperature drop across the turbine. With these temperature differences at the turbine outlet, the energy balance between the data and the simulation lead to prominent discrepancies at merge and PACK outlet stations.

The measured PACK inlet temperature is introduced as the inlet boundary condition in the simulation model. The simulation provides the estimate for the PV outlet temperature and suggests that the temperature remains constant through the PV. Temperature data was not collected at PV outlet, instead, the measurement of the temperature was taken at pTCV, which corresponds to the location immediately downstream of the TCV bypass. Since the TCV flow extraction has no impact on the temperature, the measurement at the pTCV station represents the PV outlet temperature. The data suggests that as the flow travels through the PV and approaches the pTCV station, it has a marginal (2K) drop in its temperature, which can be attributed to heat loss. However, the simulation is based on the assumption that these losses are negligible and can be safely omitted.

Downstream of the pTCV station, the flow enters the PHX, which significantly cools the air by using the ram flow as a heat sink. It can be seen that the temperature drop

across the PHX is well matched by the simulation. Note, the ram flow for the simulation is introduced in the model based on the measured ram mass flow data, and as shown Figure 12(b) the incorporated ram mass flow simulation values were maintained exactly the same as the ones measured for the corresponding cases. This suggests that the effectiveness maps incorporated in SESAC are a good representation of the performance characteristics of the aircraft PHX. This trend remains for all the heat exchangers throughout the PACK, i.e. SHX, RHX, and CHX, as the simulation estimates the change in temperature across all heat exchangers quite accurately, as shown in Figure 16(a). Figure 17 presents the acquired effectiveness values for all the heat exchangers for the simulation against the data; good agreement between experimental data and simulation is observed.

In terms of the pressure drop across the heat exchangers, Figure 18 presents the simulation estimates for the pressure drop across the heat exchangers against the data. The measured value for the SHX is not included, as the pressure is not measured there. The simulation reasonably captures the pressure drop across the RHX and CHX, implying that the implemented pressure loss coefficients are reasonable, and may require some fine tuning for the CHX. With regards to the PHX, the simulation over predicts the pressure drop by 3.75% relative to the data. Which implies that the employed friction coefficient may require some fine tuning in order to match the pressure drop. Another reason for the over prediction could also be due to the differences in the core mass flow (simulation being 3.9% higher) between the simulation and the data. It is interesting to note that, although the PHX and SHX are identical units in terms of their design, size, and shape, the pressure drop across the SHX is significantly lower relative to the PHX. This stems from the fact that the inlet conditions of the SHX with significantly lower temperature and higher pressure relative to PHX leads to increased air density (see Eq.6) which consequently reduces the friction coefficient (see Eq.23) and influences the loss coefficient (see Eq. 24) resulting in lower pressure drop across the SHX [16], [40]. This broadly explains the pressure characteristics of the heat exchangers throughout the PACK.

$$f = \frac{\tau_w}{\frac{1}{2}\rho v^2} \qquad (23)$$

$$k = f\frac{L}{D_H} \qquad (24)$$

With regards to the differences associated with the ACM, as already established, the simulation has a 3.9% higher mass flow through the ACM. The simulation incorporates the performance maps for the compressor and turbine, which determine the ACM operating point in order to match the work balance between the compressor and turbine that are mounted on the same shaft. The maps corresponding to the B737-400 aircraft could not be attained due to propriety reasons, therefore the simulations were conducted based on readily available maps incorporated for the simulation of the B737-800 PACK [16]. This can be one of the likely reason along with the differences in the mass flow through ACM that the acquired performance characteristics of the ACM could not be matched consistently against the data in terms of temperature and pressure. The simulation over predicts the compressor pressure ratio, which stems from the fact that due to higher mass flow through the turbine, the power produced by the turbine to drive the compressor is significantly higher than required. Without having representative maps for the AMC these differences in the mass flow and pressure are inevitable from the simulation point of view. Note, a good agreement is attained between the simulation and data in terms of the temperature rise across the compressor. The engineering explanation behind why the over prediction of the compressor pressure does not consistently lead to over prediction of temperature rise through the compressor is not understood. The differences in the pressure at the compressor outlet is found to propagate through the high pressure HPWS i.e. RHX, CHX.
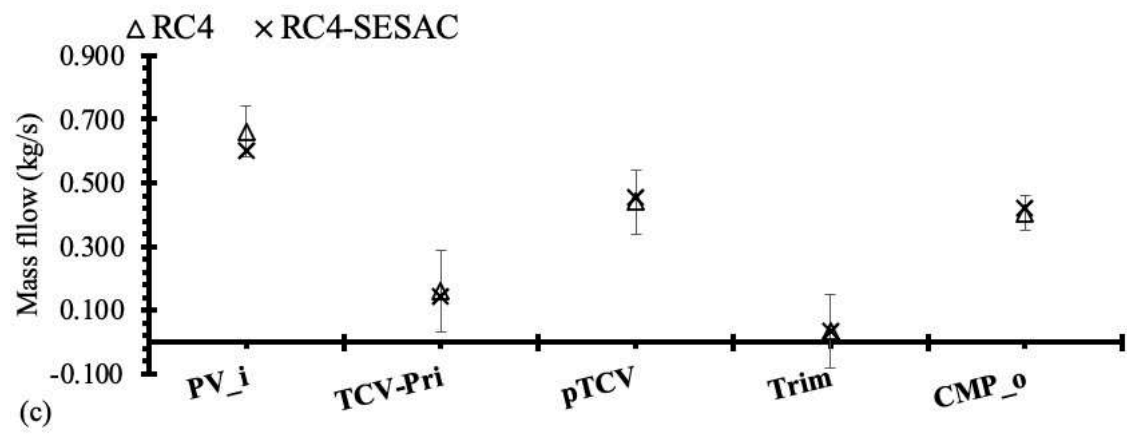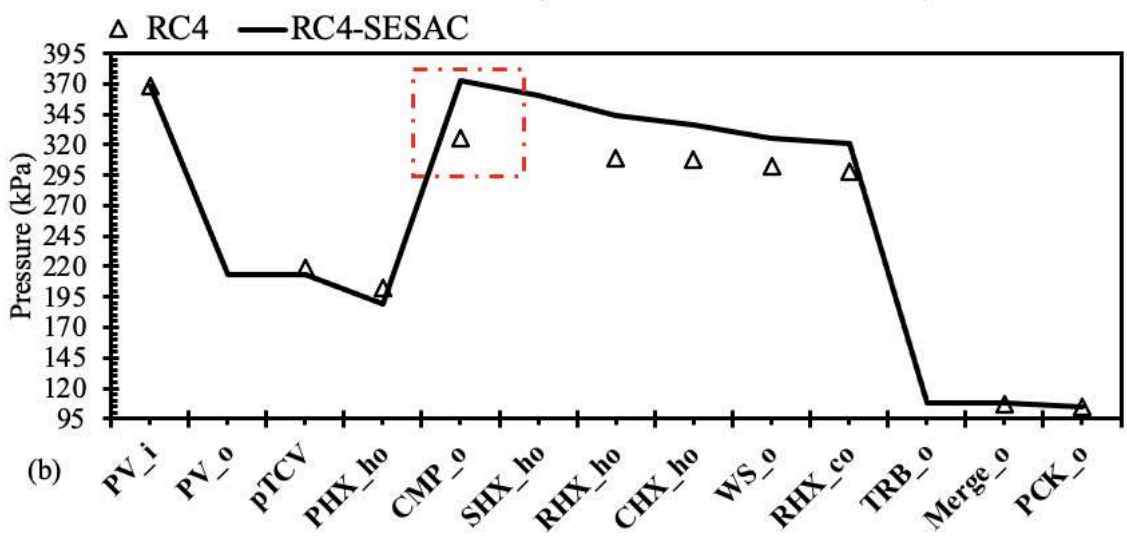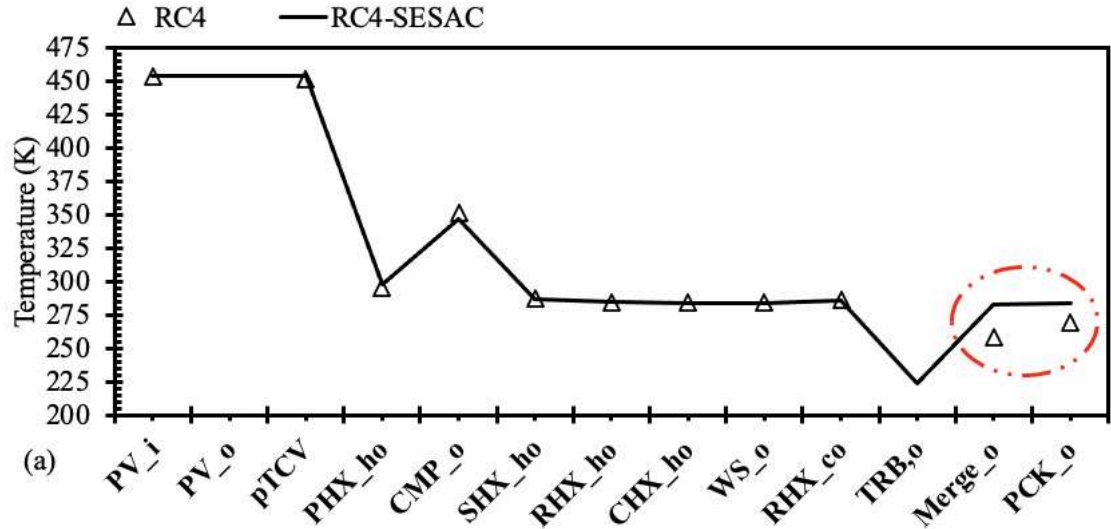
Figure 16 (a) Temperature profile, (b) Pressure profile and (c) Mass flow for RC4
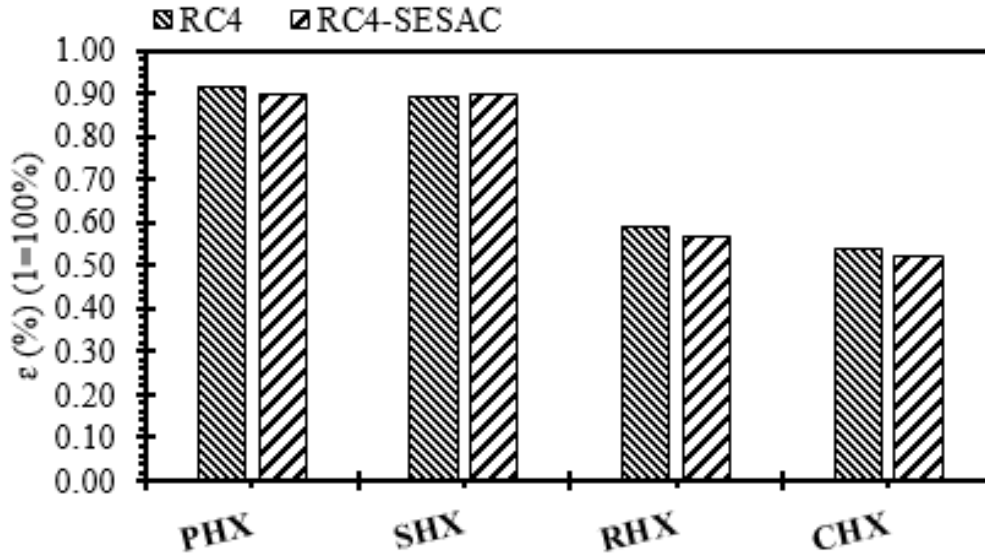
Figure 17 Effectiveness calculated using data and simulation for the heat exchangers
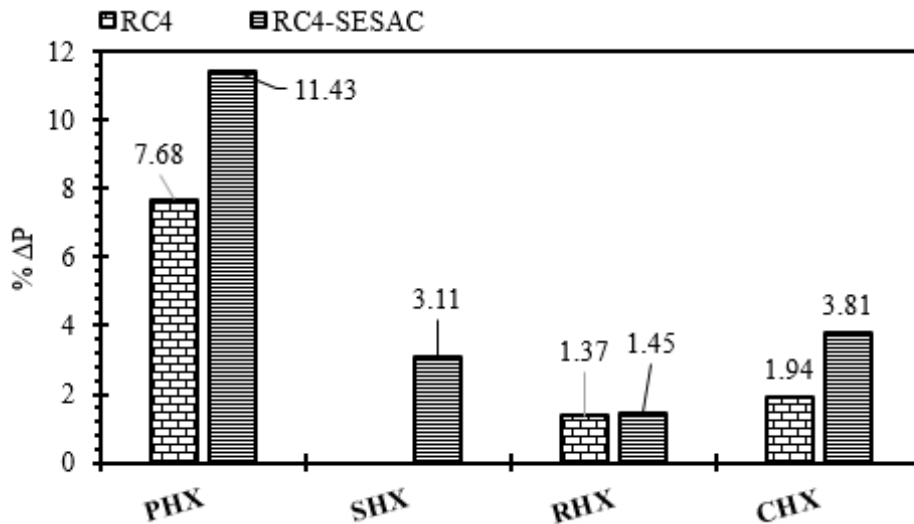

Figure 18 Experimental and simulated pressure drop across the heat exchangers

7 Summary and Conclusions

In this paper the development of a novel in-situ ground test facility for the experimental investigation of a civil aircraft ECS has been reported. The Cranfield University's ground demonstrator aircraft B737-400 has been instrumented with temperature, pressure, humidity, valve rotary sensors, and data acquisition unit. The validation of the GTF for generating temperature, pressure and mass flow data has been demonstrated based on

the data repeatability and consistency tests conducted under different ambient conditions and PACK operating modes. The installed sensor measurement uncertainly and its propagation has been thoroughly evaluated and incorporated as part of the overall data acquisition process.

The outcome of the sensor uncertainly analysis suggests that the temperature sensors have very low measurement uncertainly compared to the pressure sensors. The error propagation from these pressure transducers results in a higher uncertainty in mass flow measurement due to the use of multiple sensors, and therefore it has been identified that differential pressure transducers should be considered in order to enhance the overall measurement uncertainly. Installation of the pitot probes for the ram mass flow measurements failed to provide usable data due to their installation at the inlet of the PHX, a pitot static tube installed in the ram duct is deemed to address this shortfall.

The acquired data from the repeatability and consistency test suggest that the GTF is able to generate data that captures PACK components functional outputs under different ambient conditions and operating modes. The acquired temperature, pressure and mass flow data is found to obey the first principles of physics associated with the PACK components design and integration. The engineering characteristics of the PACK operation in terms of the control system logic for TCV and trim mass flow are found to be consistently captured by the GTF under the consistency tests. However, the control of the WS_o outlet temperature could not be captured by the GTF under both repeatability and consistency tests. The elaboration of acquired data for repeatability and consistency therefore strongly emphasize that without insights on the inbuilt control logic of the WS_o temperature regulation and the performance characteristics of the upstream and downstream systems (i.e. bleed air, mixing manifold, air distribution, and trim system) a systematic repeatability and consistency of the PACK control characterises cannot be attained.

From the PACK experimental investigation perspective, one of the key learning resulted from this study is the realisation of the role of upstream, downstream systems, and the PACK-zone controller on the PACK components performance characteristics. The second key learning is towards the realisation of the impact of trim system on the

performance characteristics of the PACK core components specifically the ACM. The trim system can substantially impact the amount of compression and expansion through the ACM and therefore the amount of cooling that can be attained under given PACK demand. The tests conducted for trim system under various PACK demands suggest that the trim system under cold demand have no practical implication on the PACK performance and can therefore be maintained off. However, under the hot demand cases, having the trim system on can influence the performance characteristics of the PACK which favours the PACK ACM to operate compatibly under hot demand.

The acquired data is further compared against the estimates of PACK performance characteristics (i.e. temperature, pressure and mass flow) under various PACK operating modes derived based on a physics based simulation model (SESAC). The estimates acquired from the simulation were found to be in good agreement with the data in terms of the temperature throughout the PACK except for the merge outlet and pack outlet temperature stations. With regards to the pressure, the required results suggest that the pressure characteristics of the components mounted upstream of the compressor are in reasonable agreement with the data, however due to inevitable differences in the incorporated ACM components performance maps, the compressor and the downstream components pressure characteristics could not be well aligned against the data. Overall, the maximum average relative difference between the simulation and data in terms of T, P and $\dot{m}$ across all reference cases is found to be 2%, 8% and 6% respectively. This was deemed as best match between the simulation and the data, as it leads to a perfect agreement for temperature throughout the core components of the PACK, as well as a reasonably acceptable match for the pressure considering the limitations associated with the resolution of the incorporated turbomachinery maps.

8 Acknowledgements

References

Figuero, D. V., 2017, "Diagnostic Capability for Environmental Control Systems." Masters dissertation, Cranfield University, Cranfield, United kingdom.

[2]   Wright, S., Andrews, G., and Sabir, H., 2009, "A review of heat exchanger fouling in the context of aircraft air-conditioning systems, and the potential for electrostatic filtering." Applied Thermal Engineering, 29(13), 2596–2609. https://doi.org/10.1016/j.applthermaleng.2009.01.002

[3]   Ma, J., Lu, C., and Liu, H., 2015, "Fault diagnosis for the heat exchanger of the aircraft environmental control system based on the strong tracking filter." PLOS ONE, 10(3). https://doi.org/0.1371/journal.pone.0122829.

[4]   Jonsson, G. R., Lalot, S., Palsson, O. P., and Desmet, B., 2007, "Use of extended Kalman filtering in detecting fouling in heat exchangers." International Journal of Heat and Mass Transfer, 50(13-14), 2643–2655. https://doi.org/10.1016/j.ijheatmasstransfer.2006.11.025.

[5]   Jonsson, G., and Palsson, O. P., 1994, "An application of extended Kalman filtering to heat exchanger models." Journal of Dynamic Systems, Measurement, and Control, 116(2), 257–264. https://doi.org/10.1115/1.2899218.

[6]   Santos, A. P. P., Andrade, C. R., and Zaparoli, E. L., 2014, "A thermodynamic study of air cycle machine for Aeronautical Applications." International Journal of Thermodynamics, 17(3), 117. https://doi.org/10.5541/ijot.538.

[7] Ma, Z., Zhang, X., Wang, C., Yang, H., and Yang, C., 2015, "Study on ground-test simulation method of the Ram Air for commercial airliners' Environmental Control System." Procedia Engineering, 121, 325–332. https://doi.org/10.1016/j.proeng.2015.08.1075.

[8]   Chowdhury, S. H., Ali, F., and Jennions, I. K., 2023, "A review of Aircraft Environmental Control System Simulation and Diagnostics." Proceedings of the Institution of Mechanical Engineers, Part G: Journal of Aerospace Engineering, 095441002311544. https://doi.org/10.1177/09544100231154441.

[9]   Burroughs, J. D., and Hammond, R. A., 1983, "Control Analysis and design features of EASY5." American Control Conference. https://doi.org/10.23919/ACC.1983.4788072.

[10]   Steinkellner, S., Andersson, H., Gavel, H., and Krus, P., 2009, "Modeling and simulation of Saab Gripen's Vehicle Systems." AIAA Modeling and Simulation Technologies Conference. https://doi.org/10.2514/6.2009-6134.

[11]   Müller, C. Scholz, D. Giese, T., 2007, "Dynamic Simulation of Innovative Aircraft Air Conditioning," 1st CEAS European Air and Space Conference, pp. 869–878.

[12]   Scholz, D. Christian, M. Giese, T. and Erdmann, C., 2007, "Flecs : Functional Library of the Environmental Control System – a Simulation Tool for the Support of Industrial Processes," AST 2007 Workshop on Aircraft Technologies.

[13]   Tu, Y. and Lin, G., 2010, "Dynamic Simulation of Humid Air Environmental Control System," 40th International Conference on Environmental Systems, pp. 1–10, https://doi.org/10.2514/6.2010-6305.

[14]   Tu, Y. and Lin, G. P., 2011, "Dynamic Simulation of Aircraft Environmental Control System Based on Flowmaster," Journal of Aircraft, vol. 48, no. 6, pp. 2031–2041. https://doi.org/10.2514/1.C031433.

[15]   Steinkellner, S., 2011, "Aircraft vehicle systems modeling and simulation under uncertainty," LINKÖPING Universuty.

[16]   Jennions, I., Ali, F., Miguez, M. E., and Escobar, I. C., 2020, "Simulation of an aircraft environmental control system," Applied Thermal Engineering, vol. 172, p. 114925. https://doi.org/10.1016/j.applthermaleng.2020.114925.

[17]   Jennions, I., Ali, F., 2021, "Assessment of Heat Exchanger Degradation in a Boeing 737-800 Environmental Control System," Journal of Thermal Science and Engineering Application, vol. 13, no. 6, Dec. 2021. https://doi.org/10.1115/1.4050324.

[18]   Childs, T., Jones, A. B., and Chen, R., 2015, "Development of a Full Scale Experimental and Simulation Tool for Environmental Control System Optimisation and

Fault Detection," 53rd AIAA Aerospace Sciences Meeting, January 5-9, 2015. https://doi.org/10.2514/6.2015-1196.

[19]   Esperon-Miguez, M., Jennions, I. K., Escobar, I. C., and Hanov, N., 2019, "Simulating faults in a Boeing 737-200 Environmental Control System using a thermodynamic model," International Journal of Prognostics and Health Management, vol. 10, no. 2, pp. 1–12. https://doi.org/10.36001/ijphm.2019.v10i2.2731.

[20]   Boon, T., 2020, "How Many Boeing 737 Aircraft Are Currently In Service & Stored?," accessed December 30, 2021, https://simpleflying.com/boeing-737-in-service-stored/.

[21]   Chowdhury, S.H., Fakhre, A., and Jennions, I. K., 2022, "Boeing 737-400 Passenger Air Conditioner Control System Model for Accurate Fault Simulation," ASME Journal of Thermal Science and Engineering Application, pp. 1–18. https://doi.org/10.1115/1.4053740.

[22]   "Boeing 737-300/400/500 Aircraft Maintenance Manual, D6-3758.".

[23]   Chowdhury, S.H., Fakhre, A., and Jennions, I. K., 2019, "A Methodology for the Experimental Validation of an Aircraft ECS Digital Twin Targeting System Level Diagnostics," Proceedings of the Annual Conference of the PHM Society 2019, Sepetember, 2019, pp. 1–11. https://doi.org/10.36001/phmconf.2019.v11i1.888.

[24]   Omega, 2021, "Temperature Isolation Coil for G1/4 & 1/4 NPT Pressure Sensor," accessed December 14, 2021. https://www.omega.co.uk/pptst/PXM-COIL.html.

[25]   Appmeas, 2021, "How can you protect sensors against high-temperature media?," accessed Dec. 14, 2021, https://appmeas.co.uk/resources/pressure-measurement-notes/how-can-you-protect-sensors-against-high-temperature-media/.

[26]   H. I. Inc., 2021 "PX2 Series Heavy Duty Pressure Transducers," accessed December 14, 2021, https://www.mouser.co.uk/datasheet/2/187/honeywell_sensing_heavy_duty_pressure_px2_series_d-2821546.pdf.

[27]   Omega, 2021, "Pt100 RTD & Thermocouple Probes for Industrial Applications," accessed Dec. 14, 2021, https://br.omega.com/omegaFilesUK/temperature/pdf/T3PROBES.pdf ().

[28]   TE Connectivity, 2021, "HTM2500LF – Temperature and Relative Humidity Module," accessed December 14, 2021 https://www.te.com/usa-en/product-CAT-HSA0001.html?q=&d=483080&type=products&samples=N.

[29]   Kirkup, L. and Frenkel, R. B., 2006, An Introduction to Uncertainty in Measurement. Cambridge: Cambridge University Press. https://doi.org/10.1017/CBO9780511755538

[30]   Variohm, 2016, "Working Principal of a Pressure Sensor,". https://www.variohm.com/news-media/technical-blog-archive/working-principle-of-a-pressure-sensor.

[31]   UMD, "Random vs Systematic Error," University of Maryland. https://www.physics.umd.edu/courses/Phys276/Hill/Information/Notes/ErrorAnalysis.html.

[32]   Solinst, 2021, "Understanding Pressure Sensor Accuracy, Precision, Resolution & Drift," accessed November 23, 2021, https://www.solinst.com/onthelevel-news/water-level-monitoring/water-level-datalogging/understanding-pressure-sensor-accuracy-precision-resolution-drift/.

[33]   Inc., H. I., 2018, "Auto-Zero Calibration Technique for Pressure Sensors." pp. 1–10, 2018, [Online]. https://sensing.honeywell.com/auto-zero-calibration-technique-pressure-sensors-technical-note.pdf.

[34]   Peters, C. A., 2001 "Statistics for Analysis of Experimental Data," Environmental Engineering Processes Laboratory Manual, S. E. Powers, Ed. AEEESP, 2001.

[35]   Taylor, J. R., 1998, An Introduction to Error Analysis: The Study of Uncertainties in Physical Measurements, Second. University Science Books.

[36]   Kim, H.-Y., 2013 "Statistical notes for clinical researchers: assessing normal distribution (2) using skewness and kurtosis," Restor. Dent. Endod., vol. 38, no. 1, p. 52, 2013, https://doi.org/10.5395/rde.2013.38.1.52.

[37] Mishra, P., Pandey, C., Singh, U., Gupta, A., Sahu, C., and Keshri, A., 2019, "Descriptive statistics and normality tests for statistical data," Ann. Card. Anaesth., vol. 22, no. 1, p. 67. https://doi.org/10.4103/aca.ACA_157_18.

[38]   Harvard University Department of Physics, "A Summary of Error Propagation," 2007.http://ipl.physics.harvard.edu/wpuploads/2013/03/PS3_Error_Propagation_sp13.pdf.

[39]   Skliros, C., Ali, F., and Jennions, I., 2020, "Experimental investigation and simulation of a Boeing 747 auxiliary power unit," ASME Journal of Engineering for Gas Turbines and Power, Vol. 142, no. 8, 2020, https://doi.org/10.1115/1.4047771.

[40]   Luyben, W. L., and Tuzla, K., 2010. "Gas Pressure-Drop Experiment," Chem. Eng. Educ., pp. 183–188, [Online]. Available: https://eric.ed.gov/?id=EJ935038.

2023-06-12

Development of a novel ground test facility for aircraft environmental control system

Chowdhury, Shafayat Hasan

American Society of Mechanical Engineers